

# Rayleigh-Taylor, Kelvin-Helmholtz and immiscible to miscible quenching instabilities in binary Bose-Einstein condensates

R. Kishor Kumar,<sup>1</sup> S. Sabari,<sup>2</sup> Arnaldo Gammal,<sup>3</sup> and Lauro Tomio<sup>2,4</sup>

<sup>1</sup>*Department of Physics, Centre for Quantum Science,  
and Dodd-Walls Centre for Photonic and Quantum Technologies,  
University of Otago, Dunedin 9054, New Zealand.*

<sup>2</sup>*Instituto de Física Teórica, Universidade Estadual Paulista (UNESP), 01140-070 São Paulo, SP, Brazil*

<sup>3</sup>*Instituto de Física, Universidade de São Paulo, 05508-090 São Paulo, SP, Brazil*

<sup>4</sup>*International Physics Center, Institute of Physics,  
University of Brasilia, 70910-900 Brasília, DF, Brazil*

(Dated: March 20, 2025)

We investigate three kinds of instabilities in binary immiscible homogeneous Bose-Einstein condensate, considering rubidium isotopes  $^{85}\text{Rb}$  and  $^{87}\text{Rb}$  confined in two-dimensional circular box. Rayleigh-Taylor (RT) and Kelvin-Helmholtz (KH) instability types are studied under strong perturbations. Without external perturbation, instabilities are also probed by immiscible to miscible quenching transition (IMQT), under two different initial configurations. Our numerical simulations show that all such instability dynamics are dominated by large vortex productions and sound-wave (phonon) propagations. For long-term propagation, vortex dynamics become dominant over sound waves in the KH instability, while sound wave excitations predominate in the other cases. For all the dynamical simulations, the emergence of possible scaling laws are investigated for the compressible and incompressible parts of the kinetic energy spectra, in terms of the wave number  $k$ . The corresponding results are compared with the classical Kolmogorov scalings,  $k^{-5/3}$  and  $k^{-3}$ , for turbulence, which are observed in the kinetic energy spectra at some specific time intervals. Deviating from the classical scaling, a kind of "Bottleneck effect" is noticed in the IMQT spectra.

## I. INTRODUCTION

In classical fluid dynamics, two regimes can be characterized by the flow of a fluid, being laminar or turbulent. The first occurs when viscous forces dominate leading to smooth and constant motion, with the turbulent flow dominated by inertial forces, creating vortices, chaotic eddies, and instabilities. The Reynolds number serves as a guide to measuring the effect of fluid friction and viscosity in the fluid, being low for constant smooth fluid motion (laminar) and high for the case the flow is turbulent [1–3]. Most flows observed in nature and physical systems are turbulent. The structure of turbulence in classical incompressible fluids was originally proposed by Kolmogorov [4] in 1941 as related to large Reynolds numbers. This and other studies by Kolmogorov on turbulence are detailed in a review by Frisch [5], together with the related investigations by several other authors. In quantum fluids, such as superfluid helium and Bose-Einstein condensate (BEC) atomic systems, turbulent motions have emerged as a new interdisciplinary research topic, named quantum turbulence (QT) in the literature [6]. For an ideal zero-temperature superfluid, the problem in the characterization of turbulence by the Reynolds number [7] was discussed in Refs. [8, 9], in which the authors define a superfluid Reynolds number via dynamical similarity, to identify a regime transition to turbulence. Also by considering heat transport and thermal waves in laminar and turbulent superfluid helium [10], a quantum analogous Reynolds number for the transition to superfluid turbulence was defined in Ref. [11], with a related discussion

in the context of BEC formalism in Ref. [12]. Currently, the studies on QT can be followed by several available works and reviews [13–19], recently updated in Ref. [20]. The quite recent works reported in Refs. [21–23] are also indicative of the actual interest in the analyses of QT in BEC. Some related numerical analyses and benchmark high-performing computer simulations are provided in Refs. [24, 25]. Turbulence is associated with stochastic movements of vortices in a fluid, whose properties differ in classical and quantum physics. Therefore, it is rooted in the fundamental differences in how vorticity behaves in these two regimes. In the quantum regime, vortices have quantized circulation, and the flow have negligible viscosity. Vortices do not decay by viscous diffusion but through other mechanisms like reconnections and phonon emission. In the classical regime, vortices can have any circulation value, and vorticity decays through viscous diffusion, leading to the dissipation of turbulent energy. These differences make quantum turbulence a fascinating area of study, with implications for understanding superfluidity, quantum fluids, and the behavior of matter at very low temperatures.

The first experimental observation of QT was reported by considering the  $^4\text{He}$  superfluid [26], with more recent experiments being extended to atomic BECs [27–30]. The BEC experiments and related studies have received significant attention due to the advanced techniques available in cold-atom laboratories, which allow precise control over the condensate parameters. For instance, in BEC researchers can manipulate the trapping potential, interaction strength, and temperature with high accuracy, enabling detailed studies of quantum tur-

bulence. The characterization of a turbulent fluid occurs through spectral analysis, with the energy being distributed across different length scales, whereas in a non-turbulent fluid, there is no significant energy transfer across scales. The evolution of large clusters with  $^{87}\text{Rb}$  BECs has been demonstrated in experiments reported in Ref. [31], with large-scale flow from turbulence being studied experimentally by considering a two-dimensional (2D) superfluid [32]. Identified in the energy spectrum of these experiments, the emergence of the classical Kolmogorov's scaling [4] was also previously observed in studies on turbulence at low-temperature superfluid flows [33]. These experiments collectively advance our understanding of quantum turbulence, bridging the gap between classical and quantum fluid dynamics. The observation of Kolmogorov's scaling in these systems is particularly noteworthy, as it suggests that some aspects of turbulence are universal, transcending the classical and quantum divide.

Further, theoretical studies on QT have been established by using appropriate versions of the mean-field Gross-Pitaevskii (GP) formalism, as one can follow from Refs. [33–36]. In this regard, one should note that, in the kinetic energy spectrum over the wave number  $k$  of quantum fluids, the occurrence of inverse energy cascade phenomenon was clearly verified in Refs. [37, 38], through the analyses of QT in forced 2D, and related signatures of coherent emerging vortex structures. Consistently with Kolmogorov's scaling, the vortex dynamics follow a  $k^{-5/3}$  power law in the infrared region of the spectrum and  $k^{-3}$  in the ultraviolet region. Such scaling laws provide insights into the nature of energy transfer in QT, with large-scale vortices dominating the dynamics in the infrared region, while the  $k^{-3}$  scaling in the ultraviolet region indicates a turbulent cascade similar to that observed in classical turbulence, where energy is transferred from larger to smaller scales.

Meanwhile, the ongoing experimental studies with binary atomic mixtures and hyperfine spin states of the same atom [39] provide motivations to extend such studies to turbulence and vortex patterns in BEC multi-component mixtures. They are of great interest due to the miscibility properties [40, 41]. In particular, the phase-separated binary mixtures show a rich variety of pattern formations, recognized as similar to the classical Rayleigh-Taylor (RT) [42, 43] and Kelvin-Helmholtz (KH) [44, 45] instabilities. The RT instability is overviewed in Ref. [46] and more recently in Ref. [47]; whereas the KH was first studied by considering instability in superfluids [48, 49]. When considering BEC mixtures, the studies on these instabilities can be followed by plenty of works from the last two decades up to now, exemplified by Refs. [50–61]. From classical fluid experiments, RT instabilities are known to start at the interface between two plane-parallel immiscible fluids under the gravity field, with the denser fluid layer at the top of the less dense one. As the equilibrium is broken, the fluid at the top moves downward, with an equal volume of the

lighter one pushing upward, resulting in mushroom head formations of the denser fluid inside the space first occupied by the less dense one. Distinguishable from RT, the KH instabilities occur when there is a difference in speed between the two fluids at the interface. These instabilities are investigated theoretically by using mean field and Bogoliubov theories. Analytical tools are developed to study the dynamic stabilization of the RT instability. However, no extensive studies discuss the QT for homogeneous binary immiscible mixtures from the perspective of analyzing Kolmogorov's spectrum, which could reveal some relation between QT and classical turbulence. In conjunction with Kolmogorov turbulence, a recent study was also reported in Ref. [61], by considering a strongly stirred immiscible mixture of two-components, in which the authors extract power-law behaviors associated to the highly or slightly immiscible conditions.

Given current cold-atom experimental activities on dipolar systems (see [62], on the observation of dipolar molecules, and references therein), some of us have also considered QT in dipolar BECs, generated by an external penetrable Gaussian-type circularly moving obstacle that produces vortex-antivortex pairs [63], following related studies with linearly-moving obstacles [64]. Along these lines, binary BEC mixtures have also been studied with the assumptions of mass-imbalanced components confined in quasi-two-dimensional (quasi-2D) pancake-like trap potential slightly perturbed elliptically by a time-dependent periodic potential [60, 65]. In the analysis of turbulence in mixtures of quantum fluids when considering quantized vortices [10], another aspect of interest is to identify the complexity by the corresponding fractal dimensions and scale distributions [66, 67], which can also be done by following some classical investigations [68, 69].

In this work, our aim is to perform numerical investigations on the emergence of instabilities and quantum turbulence in binary BEC mixtures confined in a quasi-2D circular box, considering different possible initial conditions for the mixture. Particular aspects in the dynamics of each kind of instabilities that we are reporting may demand further deep-focused investigation beyond our present work's scope. Within our numerical simulations, we have assumed the coupled  $^{85}\text{Rb}$ - $^{87}\text{Rb}$  system. However, the corresponding results can be easily extended to other coupled binary mixtures, as well as to coupled spinor states of the same atomic species, such as the recently reported experiments on RT instability considering hyperfine states of  $^{23}\text{Na}$  [70]. By assuming initial immiscible conditions, with interspecies interactions larger than the intraspecies ones, homogeneous density distributions will be considered for both spatially trapped separated components.

In our following studies of RT and KH kinds of instabilities, the same initial ground-state configurations are assumed, with the mixtures kept in immiscible regimes along the time evolution. The RT instability is triggered by introducing an initial time-independent sinusoidal perturbation in the ground-state solution (previ-

ously prepared in imaginary time). The perturbation in the real-time evolution is introduced along the interface between the components, applied to one of the species over a short time interval. The simulation follows with the sinusoidal perturbation replaced by constant linear forces applied to both components in opposite directions, breaking the stability of the interface between the immiscible fluids. For the KH instability, to simulate the difference in speed between the two classical fluids at the interface, linear constant forces are applied to both condensed species in opposite directions, parallel to the interface between the immiscible mixture.

Next, by extending our binary instability analyses, we try to distinguish the above two cases, in which external linear forces are responsible for the dynamics, from cases in which the dynamical instabilities are due to sudden variations of the nonlinear interactions. Therefore, in this third approach, we investigate the dynamical response of the system under an immiscible to a miscible quenching transition (IMQT), in which the two-body scattering length suffers a sudden reduction. For that, two possible initial space-separated configurations are assumed for the coupled system. The interest in this case also follows previous studies on phase separation and modulation instabilities with two-component atomic systems [71–75].

As it will be shown, all the above prescribed instabilities introduced in the binary BEC mixture induce plenty of vortex dipoles and turbulent flow in the condensates. To analyze them and understand how these instabilities are developed in the binary mixtures, we calculate the corresponding compressible and incompressible kinetic energy parts of the spectrum, by following an approach detailed in Ref. [76]. As it is known, in a fluid mixture, the compressible part is associated to density fluctuations and production of sound waves (phonons), whereas the incompressible part is associated to vortex dynamics and rotational motion, such that their analyses can provide information on possible universal scaling laws, which could bring consistency with the classical Kolmogorov's scaling for turbulence, as the studies provided in Ref. [37].

In the next Sect. II, the coupled GP mean-field model formalism is being described together with the corresponding expressions for the kinetic energy spectrum decomposition. The instability simulations are described and discussed in Sect. III, by considering the RT and KH instabilities generated by external forces, together with IMQT instabilities obtained by sudden changes in the miscibility of the coupled system. Finally, a summary with main conclusions are given in Sect. IV.

## II. MEAN-FIELD MODEL FOR BINARY BEC CONFINED IN A UNIFORM CIRCULAR BOX

In our approach for the coupled BEC system, we are assuming a quasi-2D pancake like configuration, with two atomic species (identified by  $i = 1, 2$ , with masses  $m_i$ ) having the same number of atoms  $N_i \equiv N$ , strongly con-

finied by three-dimensional (3D) harmonic traps with aspect ratios  $\lambda_i = \omega_{i,z}/\omega_{i,\perp}$ , where  $\omega_{i,z}$  and  $\omega_{i,\perp} (\equiv \omega_{i,x} = \omega_{i,y})$  are, respectively, the longitudinal and transverse trap frequencies for the species  $i$ . Given our units in terms of the lighter particle 1, in order to have both particles trapped with about the same aspect ratio  $\lambda$ , one needs  $m_1\omega_{1z}^2 = m_2\omega_{2z}^2$ , implying  $\omega_{2z}/\omega_{1z} \approx 0.99$ . So, with trap frequencies  $\omega_{i,\perp}$  being the same, given by  $\omega_{\perp} \equiv \omega_{i,\perp} = 2\pi \times 10$  Hz, we can assume  $\lambda \approx \lambda_i = 50$ , with  $\omega_{i,z} = 2\pi \times 500$  Hz. Within such constraints, with the binary system strongly confined to a pancake-like 2D shape, the original 3D formalism can be reduced to a quasi-2D one, by solving analytically the part of the Hamiltonian corresponding to the  $z$ -variable, in which the trap is given by  $V_i(z) = m_i\omega_{i,z}^2 z^2/2$ , implying in a constant factor in the 2D formalism. As the 2D system is enough strongly confined, for practical purpose in our model we replace the 2D-harmonic trap, by further assuming the coupled system confined in a uniform circular box, as it will be defined in our following formalism, and along the different model approaches we are considering. In all the simulations we are reporting, for simplicity we have assumed the intraspecies scattering lengths are identical and fixed for both species, with  $a_{11} = a_{22} = 100a_0$  ( $a_0$  is the Bohr radius), such that the relative strength between the scattering lengths is controlled by the interspecies interaction  $a_{12}$ . Actually, these setups are accessible in ultracold gases experiments by using Feshbach resonances mechanisms to tune the two-body scattering lengths [77, 78].

Following the above discussion, we have the corresponding mean-field 2D coupled GP formalism. For computational purpose, this 2D formalism is cast in a dimensionless format, with energy, time, and length units given, respectively, by  $\hbar\omega_{\perp}$ ,  $\omega_{\perp}^{-1}$ , and  $l_{\perp} \equiv \sqrt{\hbar/(m_1\omega_{\perp})}$ , with the first species being used as the reference for the length unit. Correspondingly, the space and time variables are such that  $\mathbf{r} \rightarrow l_{\perp}\mathbf{r}$  and  $t \rightarrow t/\omega_{\perp}$ , when going to dimensionless quantities. For details on how the 2D dimensionless formalism is reached for a mass-different binary system, one can analogously follow related expressions given in Ref. [79]. Therefore, the coupled 2D GP equation, for the wave-function components  $\psi_i \equiv \psi_i(x, y; t)$ , normalized to one,  $\int_{-\infty}^{\infty} dx dy |\psi_i|^2 = 1$ , is given by

$$i\frac{\partial\psi_i}{\partial t} = \left\{ \frac{-m_1}{2m_i}\nabla_2^2 + V_i(x, y) + \sum_{j=1,2} g_{ij}|\psi_j|^2 \right\} \psi_i, \quad (1)$$

where  $\nabla_2^2 \equiv \partial^2/\partial x^2 + \partial^2/\partial y^2$ . The nonlinear strengths  $g_{ij}$  refer to the contact interactions, related to the two-body scattering lengths  $a_{ij}$  (where  $a_{ij} = a_{ji}$  and we assume  $a_{11} = a_{22}$ ), which are expressed by

$$g_{ij} \equiv \sqrt{2\pi\lambda} \frac{m_1 a_{ij} N_j}{m_{ij} l_{\perp}}, \quad (2)$$

where  $m_{ij} \equiv m_i m_j / (m_i + m_j)$  is the reduced mass. In Eq. (1),  $V_i(x, y)$  is the 2D confining potential, initially

assumed with identical form for both species  $i = 1, 2$ , which will be altered by linear perturbations along our numerical simulations, as it will be detailed. So, initially, we consider  $V_i(x, y)$  as given by a uniform circular box with fixed radius  $R$  and height  $V_0$ , given by

$$V_i(x, y) = \begin{cases} V_0, & \text{for } \sqrt{x^2 + y^2} > R, \\ 0, & \text{for } \sqrt{x^2 + y^2} \leq R, \end{cases} \quad (3)$$

where  $V_0$  will be considered much larger than the dimensionless chemical potentials,  $V_0 \gg \mu_i/(\hbar\omega_\perp)$ . (With our units defined in terms of the transversal confining harmonic potential, as in Ref. [80], the consistency with approaches using the longitudinal frequency  $\omega_z$ , as Ref. [8], requires considering  $\lambda = 50$ , with  $l_\perp = \sqrt{\lambda}l_z$ ).

Next, within our specific numerical simulations, to be described in the next sections,  $V_i(x, y)$  will be altered by linear perturbations that will not have identical form for both species  $i = 1, 2$ . Along this work, together with the same number of atoms for both species, we also assume the length unit adjusted to  $l_\perp = 3.4 \mu\text{m} \approx 6.425 \times 10^4 a_0$ , where  $a_0$  is the Bohr radius, such that  $a_{ij}$  can be conveniently given in terms of  $a_0$ . The other fixed numerical factors are the size of the 2D circular box potential, defined in (3), which we assume  $R = 35$  (in units of  $l_\perp$ ), the number of atoms of both components  $N = N_i = 2 \times 10^6$  and the equal intra species interaction  $a_{ii} = 100a_0$ .

### A. Two-component miscibility

The condition to enter the immiscible regime corresponds to the one to minimize the energy [40], given by  $g_{12}^2 > g_{11}g_{22}$ , for  $N_1 = N_2$  and  $a_{11} = a_{22} > 0$  [using Eq. (2)]. This defines the threshold parameter  $\delta$ , with the immiscible necessary condition:

$$\delta \equiv \sqrt{\frac{g_{12}^2}{g_{11}g_{22}}} = \frac{m_1 + m_2}{2\sqrt{m_1m_2}} \left( \frac{a_{12}}{a_{11}} \right) > 1. \quad (4)$$

The expression at the right provides the mass-dependent critical value in terms of the ratio between inter to intraspecies two-body scattering lengths for the miscible-immiscible transition of a homogeneous mixture. In the present case, this critical value is close to the equal mass case ( $a_{12} \simeq 0.99993a_{11}$ ). A more close definition for the miscibility of two coupled system in a Bose mixture is provided by an overlap relation between the densities. In the present 2D case, with  $\psi_i$  normalized to one, the overlap can be expressed as in Ref. [41], by

$$\eta = \int |\psi_1||\psi_2| dx dy = \int \sqrt{|\psi_1|^2|\psi_2|^2} dx dy. \quad (5)$$

Another definition for the overlap, used in [72], which will be assumed in the present investigation, is given by

$$\Lambda = \frac{[\int |\psi_1|^2|\psi_2|^2 dx dy]^2}{(\int |\psi_1|^4 dx dy)(\int |\psi_2|^4 dx dy)}. \quad (6)$$

Both  $\eta$  and  $\Lambda$  definitions for the miscibility of a coupled binary system give the same results in the extremes: for complete immiscible case they are zero; and in the opposite complete miscible case,  $\Lambda = \eta = 1$ . However, to emphasize the mixture,  $\eta$  can be considered a stronger factor than  $\Lambda$ . By representing the components by two Gaussians, one can verify that  $\Lambda = \eta^2$ , such that for very different widths as with  $\eta = 0.2$ , we have  $\Lambda = 0.04$ .

### B. Kinetic energy spectrum decomposition

From the Eq. (1), the corresponding total energy for the binary system is given by

$$E(\psi_1, \psi_2) = \int dx dy \sum_i \left\{ \frac{m_1 |\nabla_2 \psi_i|^2}{2m_i} + V_i(x, y) |\psi_i|^2 \right\} + \int dx dy \sum_{i,j} \frac{g_{ij}}{2} |\psi_j|^2 |\psi_i|^2. \quad (7)$$

To analyze the turbulent behavior which can occur in the coupled system, it is appropriate to study the corresponding decomposition of the kinetic energy spectrum for the present 2D formalism, as detailed in Refs. [8, 76]. For that, in the fluid dynamics interpretation of the GP equation, we apply the Madelung transformation, such that the coupled condensate wave function is given by  $\psi_i \equiv \sqrt{n_i} \exp(i\theta_i)$ , where  $n_i \equiv n_i(x, y; t)$  is the density of the species  $i$ , with  $\theta_i \equiv \theta_i(x, y; t)$  the corresponding fluid macroscopic phase. With the fluid velocity for each component  $i$  being defined as  $\mathbf{v}_i(x, y; t) = \nabla_2 \theta_i$ , and with correspondingly density-weighted velocity given by  $\mathbf{u}_i \equiv \mathbf{u}_i(x, y; t) \equiv \sqrt{n_i} \mathbf{v}_i(x, y; t)$ , the kinetic energies of each component  $i$  of the mixture can be expressed by

$$K_i = \frac{m_1}{2m_i} \int dx dy |\mathbf{u}_i|^2. \quad (8)$$

The kinetic energy is further decomposed in compressible and incompressible parts, with the incompressible energy primarily due to the presence of quantized vortices, and the compressible energy originated from sound waves. We write this decomposition as  $\mathbf{u}_i = \mathbf{u}_{i,I} + \mathbf{u}_{i,C}$ , in which the incompressible field  $\mathbf{u}_{i,I}$  satisfies  $\nabla \cdot \mathbf{u}_{i,I} = 0$ , with the compressible field  $\mathbf{u}_{i,C}$  satisfying  $\nabla \times \mathbf{u}_{i,C} = 0$ . Therefore, the kinetic energy terms are decomposed as  $K_i = K_{i,I} + K_{i,C}$ , where the respective compressible and incompressible parts are defined as

$$\begin{pmatrix} K_{i,I} \\ K_{i,C} \end{pmatrix} = \frac{m_1}{2m_i} \int dx dy \begin{pmatrix} |\mathbf{u}_{i,I}|^2 \\ |\mathbf{u}_{i,C}|^2 \end{pmatrix}. \quad (9)$$

We can obtain these compressible and incompressible kinetic energy spectrum by considering momentum space Fourier transform, as

$$\begin{pmatrix} K_{i,I} \\ K_{i,C} \end{pmatrix} = \frac{m_1}{2m_i} \int dk_x dk_y \begin{pmatrix} |\mathcal{F}_{i,I}(k_x, k_y)|^2 \\ |\mathcal{F}_{i,C}(k_x, k_y)|^2 \end{pmatrix}, \quad (10)$$



where

$$\begin{pmatrix} \mathcal{F}_{i,I}(\mathbf{k}) \\ \mathcal{F}_{i,C}(\mathbf{k}) \end{pmatrix} = \frac{1}{2\pi} \int dx dy e^{-ik_x x - ik_y y} \begin{pmatrix} \mathbf{u}_{i,I} \\ \mathbf{u}_{i,C} \end{pmatrix}. \quad (11)$$

From Eq. (10), the total incompressible and compressible kinetic energies can be obtained by extending to two components the procedure detailed in [8]. Within this procedure, we first obtain the spectral density in  $k$ -space in polar coordinates  $(k, \phi_k)$ , with the final kinetic energies by integrating on  $k = \sqrt{k_x^2 + k_y^2}$ , as follows:

$$\begin{pmatrix} K_{i,I} \\ K_{i,C} \end{pmatrix} = \int_0^\infty dk \begin{pmatrix} \mathcal{K}_{i,I}(k) \\ \mathcal{K}_{i,C}(k) \end{pmatrix}, \quad (12)$$

where

$$\begin{pmatrix} \mathcal{K}_{i,I}(k) \\ \mathcal{K}_{i,C}(k) \end{pmatrix} = \frac{m_1 k}{2m_i} \int_0^{2\pi} d\phi_k \begin{pmatrix} |\mathcal{F}_{i,I}(k_x, k_y)|^2 \\ |\mathcal{F}_{i,C}(k_x, k_y)|^2 \end{pmatrix} \quad (13)$$

express (for both components  $i$  of the mixture) the respective incompressible ( $I$ ) and compressible ( $C$ ) kinetic energy spectrum over the wave number  $k$ .

### C. Numerical approach

For the numerical simulations, applied to the three different kinds of instabilities in BEC mixtures that we are reporting, we use the split-step Crank-Nicolson method to solve Eq. (1). It is followed by performing the Fourier transforms to reach the compressible and incompressible kinetic energy spectra. The details for the numerical calculations of the corresponding velocity power spectra can be obtained in Refs.[8, 76]. With the ground-state solutions previously prepared in the imaginary time, the dynamics are followed by real-time evolutions, in which the applied external potential and miscibility conditions are responsible for the kinds of instabilities we are investigating. The numerical simulations are carried out by using  $400 \times 400$  square grid with box length  $L_x = L_y = 80l_\perp$ , with the corresponding wave number infrared limit being  $k_L = 2\pi/L$ . The time step  $\Delta t$  is chosen to be  $10^{-3}$ . For each species, the respective healing lengths  $\xi_i$  are assumed fixed to  $\sim 0.4\mu\text{m}$ , where  $\xi_i = \sqrt{\hbar^2/(m_i\mu_i)} = l_\perp \sqrt{(m_1/m_i)(\hbar\omega_\perp/\mu_i)} \equiv l_\perp \xi$ , implying that  $\mu_2 = (m_1/m_2)\mu_1$ . As we are assuming the species have an equal number of atoms and identical intraspecies scattering lengths, only the small mass difference ( $m_1/m_2 \approx 0.98$ ) plays a role in determining the chemical potential. In addition to the different dynamics, the initial immiscible trapping conditions are quite relevant in the numerical simulations, as observed particularly in the case of instabilities obtained when considering immiscible to miscible sudden changes.

## III. INSTABILITY SIMULATIONS IN BINARY BOSE-EINSTEIN CONDENSATES

In our present study, we have investigated dynamical processes that occur with a slightly mass-imbalanced binary mixture, represented by the  $^{85}\text{Rb}$ - $^{87}\text{Rb}$  BEC system, prepared initially in immiscible space configuration. We explore instabilities analogous to the Kelvin-Helmholtz and Rayleigh-Taylor, engineered by externally applied perturbations, as well as by quenching the nonlinearity of the mixture from immiscible to miscible, called IMQT. These standard instabilities typically evolve from stationary states, where infinitesimal perturbations grow over time. This is well-studied in classical fluid dynamics and can be extended to quantum gases using the Bogoliubov-de Gennes (BdG) analysis, a standard tool for examining the onset of instabilities in quantum systems from stationary states. In our study, with the main interest in the evolution dynamics of the instabilities, we avoid the traditional approach by engineering the initial conditions to evolve the states out of equilibrium from the beginning. Specifically, the mathematical structure of our problem precludes the use of BdG analysis, prompting us to investigate these instabilities in a time-dependent framework. The motivation for this approach relies on mathematical clarity and the observation that the resulting patterns are similar to those seen in standard cases. Apart from several previous studies on this matter, noticeable are the recent experimental setups considering RT and KH instabilities in quantum fluids, as reported in Refs. [70, 81].

Next, we present numerical simulations leading to three kinds of instabilities in binary mass-imbalanced mixtures of two BEC systems, prepared in immiscible conditions. We present our simulations for the density dynamics, compressible and incompressible kinetic energies, and corresponding spectra. The first two cases refer to RT and KH kinds of instabilities, obtained by external forces keeping the same immiscible initial conditions. In the case of IMQT, which refers to sudden changes in the non-linearity of the coupled system, two kinds of initial conditions are investigated for the dynamics. Even considering that all simulations can be easily adapted to other binary atomic systems, particularly to spinor levels of the same atom, here we are assuming the mass-imbalanced  $^{85}\text{Rb}$ - $^{87}\text{Rb}$  binary BEC mixture.

For all the instabilities we have investigated, the incompressible results are expected to be dominated by the motion of quantized vortices, with the compressible parts being due to sound wave radiations, density fluctuations, and other dissipative effects. Both can follow the same scaling when strongly coupled, with energy transfer between the modes. However, they do not necessarily follow the same energy cascade process, as the kinetic compressible mode can be radiated away as sound waves or through other mechanisms. The  $k^{-3}$  scaling behavior in the kinetic energy spectrum is known to arise from the vortex core structure. This regime cannot support the

energy cascade. Conversely, the infrared regime (with wave number  $k\xi \ll 1$ ) arises purely from the configuration of the vortices and turbulence. The energy injected by the vortices and their interactions can be observed in the infrared regime, as already noticed in Ref. [8].

### A. Rayleigh-Taylor instability in coupled BECs

In normal classical fluids, the RT instability occurs at the interface between two different-density fluids. In particular, it happens when the lighter fluid pushes the heavier one with the support of the gravitational force. To simulate the occurrence of a similar effect in ultra-cold systems, instead of a gravity force acting among the two species we assume an immiscible binary mixture, in which the two elements are under the effect of external opposite linear forces acting on the two components. The mass difference between the components can be neglected, as the simulation can be done as well with two spinor levels of the same atomic species, prepared in immiscible conditions. To contemplate this model, we prepare the ground state by considering an axially phase-separated mixture, with the interspecies interaction chosen to be larger than the intraspecies one, as shown in Fig. 1 with  $\delta = 1.05$  ( $a_{12} = 105a_0$  and  $a_{11} = a_{22} = 100a_0$ ). In our simulation, the initial two-component ground-state solutions of the mixture are obtained by using imaginary-time calculations, immediately followed by their real-time evolution. In Fig. 1, the upper panels (a<sub>1</sub>) and (a<sub>2</sub>) depict the prepared initial two-component densities for the immiscible mixture at  $t = 0$ , when starting the real-time propagation. Due to numerical conditions when concluding the imaginary-time calculations and starting the real-time evolution, it happens that at  $t = 0$  the borderline separation (between the two immiscible fluids) starts slightly inclined as related to the horizontal line. Throughout the temporal evolution, the two-body scattering lengths are kept constant. To start the dynamical instability, the trap interaction (3) is modified by a sinusoidal  $x$ -direction perturbation applied to the first component for a short time interval from  $t = 0$  till  $t = 2$  (units of  $\omega_{\perp}^{-1}$ ), creating the density oscillation presented in the panels (b<sub>1</sub>) and (b<sub>2</sub>). The simulation follows (for  $t > 2$ ) with the sinusoidal perturbation removed, being replaced by a linear perturbation  $\nu_i y$ , which provides a constant force  $\nu_i$  in the  $y$ -direction. More explicitly, by using the usual Kronecker  $\delta_{i,j}$  ( $=1$ , for  $i = j$ ;  $0$ , otherwise) and the step-function  $\Theta(x)$  ( $=1$ , for  $x > 0$ ;  $0$ , for  $x < 0$ ), in this case the modified dimensionless interaction  $\tilde{V}_i$  can be written as

$$\tilde{V}_i(x, y; t) = V_i(x, y) + \nu_i y \Theta(t-2) - \delta_{i,1} \Theta(2-t) \cos\left(\frac{x}{2}\right). \quad (14)$$

For the simulation shown in Fig. 1,  $\nu_1 = 1.2$  and  $\nu_2 = -1.2$ . To develop the RT instability at the interface, the linear forces are introduced in both components, in opposite  $y$ -directions, to mimic a system under gravity field. However, with the external forces applied as prescribed, there is no need for the species having different masses; the same approach could also be applied to spinor states of the same atom. The main relevant

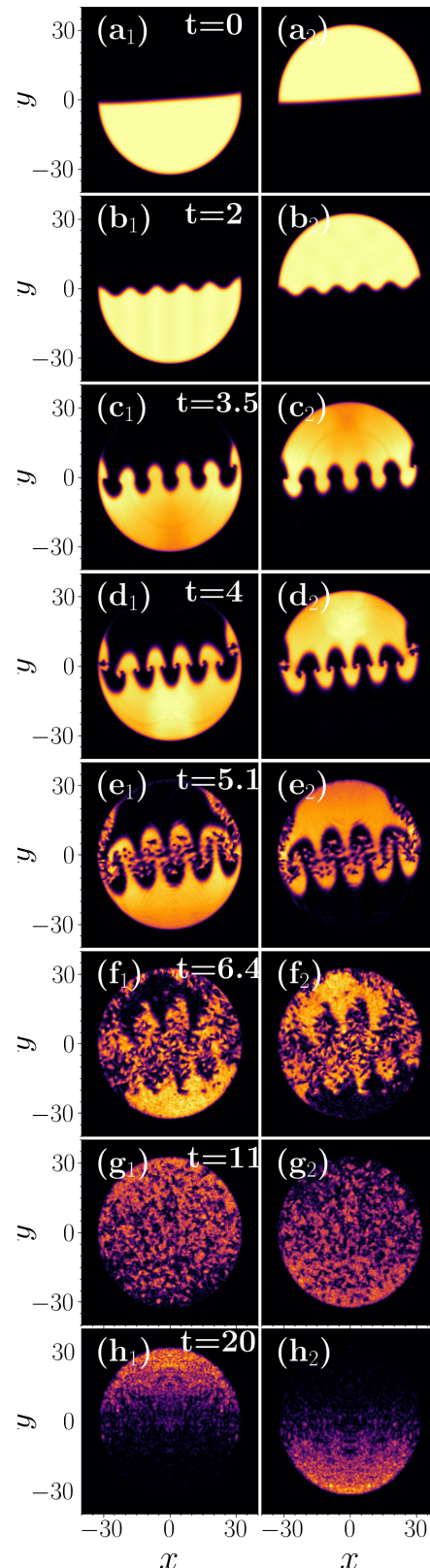


FIG. 1. RT instability in the binary mixture  $^{85}\text{Rb}$  [(a<sub>1</sub>) to (h<sub>1</sub>)] and  $^{87}\text{Rb}$  [(a<sub>2</sub>) to (h<sub>2</sub>)], showing the respective densities  $|\psi_i|^2$  at different time snapshots (indicated inside the left panels), for the immiscible condition  $\delta = 1.05$ . The units for time and length are, respectively,  $\omega_{\perp}^{-1}$  and  $l_{\perp}$ . (The full dynamics of this figure is available among the supplemental material.)

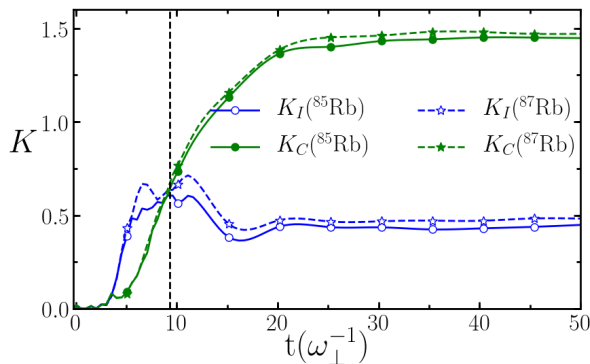


FIG. 2. (Color online) Time evolutions of incompressible and compressible kinetic energies,  $K_I$  and  $K_C$  (units  $\hbar\omega_\perp$ ), for the  $^{85}\text{Rb}$ - $^{87}\text{Rb}$  mixture, associated with RT instabilities, with convention as indicated inside the panel. The vertical dashed line at  $t \approx 9$  is identifying the approximate time instant for the energy transition from incompressible (related to the vorticity) to compressible (sound waves) dominated fluid.

requirement for starting the dynamics is the immiscibility provided by the fixed relation between the inter and intraspecies scattering lengths, which we are assuming such that  $\delta = 1.05$ .

For the mass-imbalanced mixture, we follow a previous study done in Ref. [80], in which the linear force is introduced by a small perturbation in the trap. Here, a tendency is observed for the components of the mixture to occupy distinct spaces inside the trap, moving to opposite positions as compared to the original ones. So, in a longer evolution, this behavior is evidenced by the coupled panels ( $h_i$ ), with the densities accumulated at the extreme borders.

Related experimental and theoretical proposals for applying linear perturbations have also been discussed in Refs. [51–55, 82]. Quite similar to our present numerical simulation, recently it was reported in Ref. [70] an experimental observation of RT instability in a binary quantum fluid composed of two hyperfine levels of  $^{23}\text{Na}$ , which are trapped by a square potential with minimal symmetry breaking at  $y = 0$ .

Figure 1, in the first panels ( $a_i$ ) and ( $b_i$ ) of the evolution, displays the density separations between the condensates and the sinusoidal perturbations (introduced at  $t = 2$ ), which are helpful to observe the RT instability being generated in the  $^{85}\text{Rb}$ - $^{87}\text{Rb}$  mixture. The dynamical process in the evolution follows just after the replacement of the sinusoidal perturbation by the external forces, at  $t = 2$ , with mushroom pattern formations and plenty of vortex dipoles generated under the head of the mushrooms. Together with the vortex dynamics, it can also be noticed the sound wave productions. The panels ( $c_i$ ) till ( $h_i$ ) of Fig. 1 provide indicative snapshot results of the RT instability simulation. This instability is being analyzed through our results for the kinetic energy spectrum, considering the approach presented in Sect. IIB.

As the vorticity (measured by the increasing number of vortices) is primarily associated with the increase in the

incompressible part of the kinetic energy, namely  $K_{i,I}$ , whereas the sound-wave production is related to the compressible part,  $K_{i,C}$ . The respective behaviors can be observed from the results shown in Fig. 2, for the evolution of both kinetic energies parts. Following the legends and caption of Fig. 2, the solid-blue (dashed-blue) line refers to the incompressible kinetic energy  $K_{^{85}\text{Rb},I}$  ( $K_{^{87}\text{Rb},I}$ ), whereas the solid-green (dashed-green) line refers to the corresponding compressible part,  $K_{^{85}\text{Rb},C}$  ( $K_{^{87}\text{Rb},C}$ ). As noticed, the vorticity of both components fast increases in the interval  $2 < t < 11$ , when the incompressible part of the kinetic energy is dominating the dynamics. The sound-wave production starts to increase for larger times, dominating the dynamics in the long-time evolution. It corresponds to phonon excitations in the fluid, which can be attributed to the energy transfer obtained from the dynamics of vortex-antivortex production and annihilation in a continuous process that stays for longer times [83, 84]. As the external forces are maintained along the dynamics, the  $K_{i,I}$  behaviors (related to vorticities), which have maxima near  $t = 10$ , remain higher enough for  $t > 11$ , besides being lower than the  $K_{i,C}$  (related to the large sound wave production). Therefore, the associated vortex number (not shown in this case) becomes quite large along the dynamics, being also coupled with sound wave propagations. The correspondence between the vortex number and the incompressible kinetic energies can be followed numerically more precisely when having moderate instabilities in the long-time evolution, such as the cases we are considering in the final part of the present study.

As indicated in Fig. 2, the vortex production starts near  $t \approx 3.5$  in the dynamics, with the corresponding energy  $K_{i,I}$  being greater than  $K_{i,C}$  (related to sound waves) for both components of the mixture until  $t \approx 9$ . Plenty of vortex dipoles are being generated during this time interval, with the contribution of sound waves being less significant. Once both condensate elements are forced to share their position, more sound waves start to be created, dominating the dynamics. The vertical dashed line in Fig. 2 indicates approximately the time position at which the transition occurs, from the dominance of incompressible kinetic energies (for  $t \leq 9$ ) to compressible ones (for  $t \geq 9$ ). By comparing the two species' behavior, consistently, it is noticeable that the kinetic energies for the more massive element are slightly greater than the ones obtained for the less massive element. They are enhanced particularly in the case of incompressible energies close to the time when the transition happens from incompressible to compressible dominance.

The kinetic energy spectra over the wave number  $k$  can provide a better approach for analyzing the instabilities and turbulent behaviors that can occur in the evolution. For that, we have Fig. 3, which shows results related to the dynamics presented in Figs. 1 and 2, considering four instants of interest in the onset of the instability. So, in Fig. 3 we are displaying in log scales the corre-

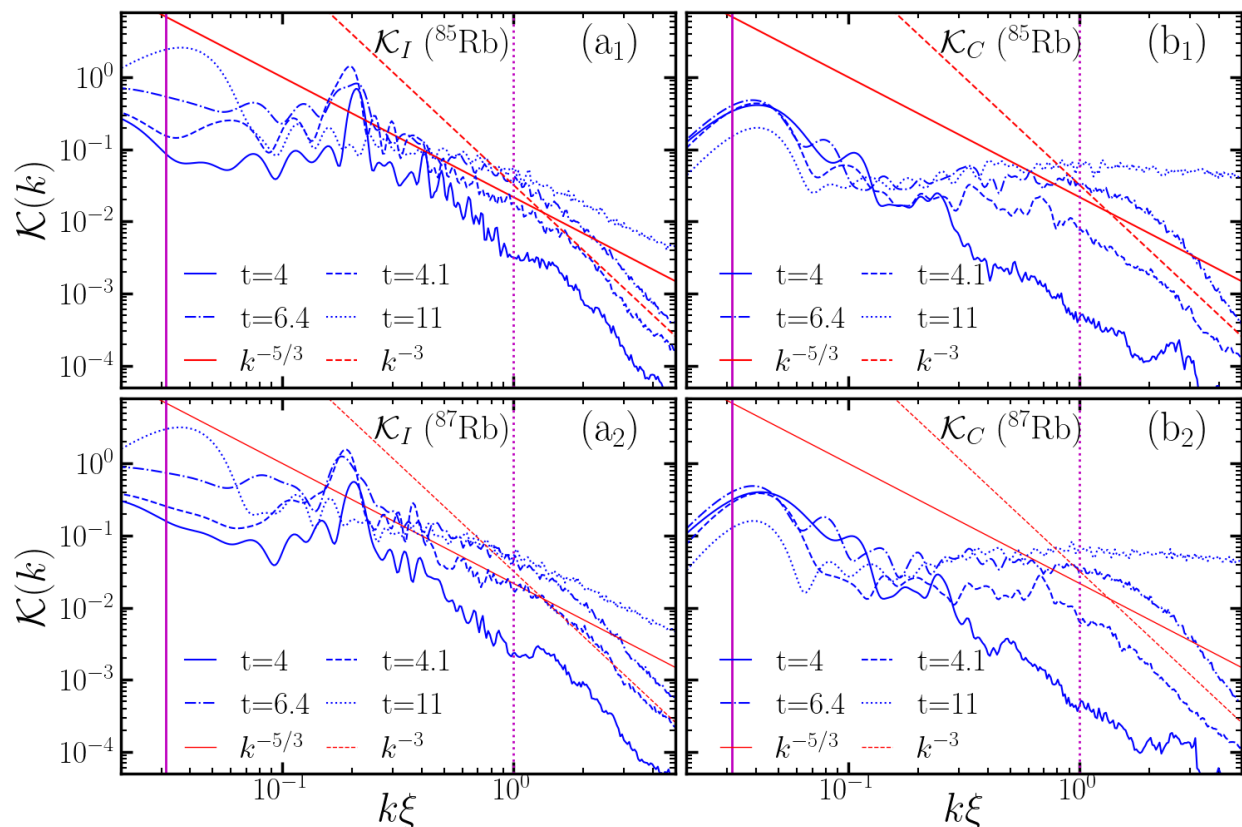


FIG. 3. (Color online) Incompressible [panels (a<sub>i</sub>)] and compressible [panels (b<sub>i</sub>)] kinetic energy spectra,  $\mathcal{K}(k)$  (units of  $\hbar\omega_{\perp}l_{\perp}$ ), for the RT instabilities, are shown as functions of the dimensionless  $k\xi$  for the  $^{85}\text{Rb}$  (upper panels) and  $^{87}\text{Rb}$  (lower panels) components of the mixture, considering four different instant times  $t$  in the evolution (as indicated). The inclined straight lines provide the  $k^{-5/3}$  and  $k^{-3}$  behaviors, for comparison. The vertical lines refer to the size of the box (infrared limit),  $k\xi = k_L\xi = 0.01\pi$  (solid line), and the starting ultraviolet region  $k\xi = 1$  (dotted line). The two closed instants 4.0 and 4.1 refer to the fast behavior transition following the panels (d<sub>i</sub>) shown in Fig. 1. The healing lengths, for both components, are assumed  $\xi \sim 0.4l_{\perp}$ , with  $k$  in units of  $l_{\perp}$ .

sponding spectral functions,  $\mathcal{K}_{i,I}(k)$  and  $\mathcal{K}_{i,C}(k)$ , given by Eq. (13), as functions of  $k\xi$ , where  $\xi$  refers to the assumed common healing lengths of both elements. The inclined straight lines inside the panels are just guidelines showing the expected classical scaling behaviors for turbulence,  $k^{-5/3}$  (red-solid line) and  $k^{-3}$  (red-dotted line), corresponding to the infrared ( $k\xi < 1$ ) and ultraviolet ( $k\xi > 1$ ) regions, respectively. The solid vertical line in the infrared regime, at  $k = k_L = 2\pi/L$ , provides the size of the box, with the dotted vertical line indicating the position where  $k = 1/\xi$ . These scalings are useful in identifying possible time intervals at which the dynamics may follow more closely the classical scalings for turbulence, such that some similarities can be traced between classical and quantum behaviors.

As shown in the four panels of Fig. 3, at which we consider four instant sample results in the onset of instability, the  $k^{-3}$  scaling behavior expected in the ultraviolet regime (for  $k\xi \gg 1$ ) can be recognized approximately close to the time interval between 4 and 6.4 (units  $1/\omega_{\perp}$ ), for both incompressible and compressible kinetic energies. This interval is consistent with the results shown in

Fig. 1 for the dynamical evolution of the densities. Deviations are noticed outside this interval, particularly for larger times of  $\mathcal{K}_{i,C}(k)$  results. By going to the ultraviolet limit, the spectrum starts to become more flattened, as noticed in the compressible results. This behavior, which can be verified for  $t > 9$ , is represented in Fig. 3 by the dotted line for  $t = 11$ . Also noticed in Fig. 2, for  $t > 9$  we start having dominance of compressible effects (sound waves and quantum fluctuations) in the dynamics. On the intermediate  $k$  region, for  $0.2 < k\xi < 1$ , we can approximately identify the  $k^{-5/3}$  behavior only in case of the incompressible kinetic energy results, (see, the results for  $t = 4.1$  and  $6.4$ ), with the results for  $t = 4.0$  and  $4.1$  indicating a transition behavior from  $k^{-2}$  to  $k^{-5/3}$ . Essentially, the incompressible results are dominated by the motion of quantized vortices, in the initial time interval. However, in this case, the compressible energies are not being transferred through a cascade process as the incompressible ones, which is understood due to sound wave radiations and dissipative effects.



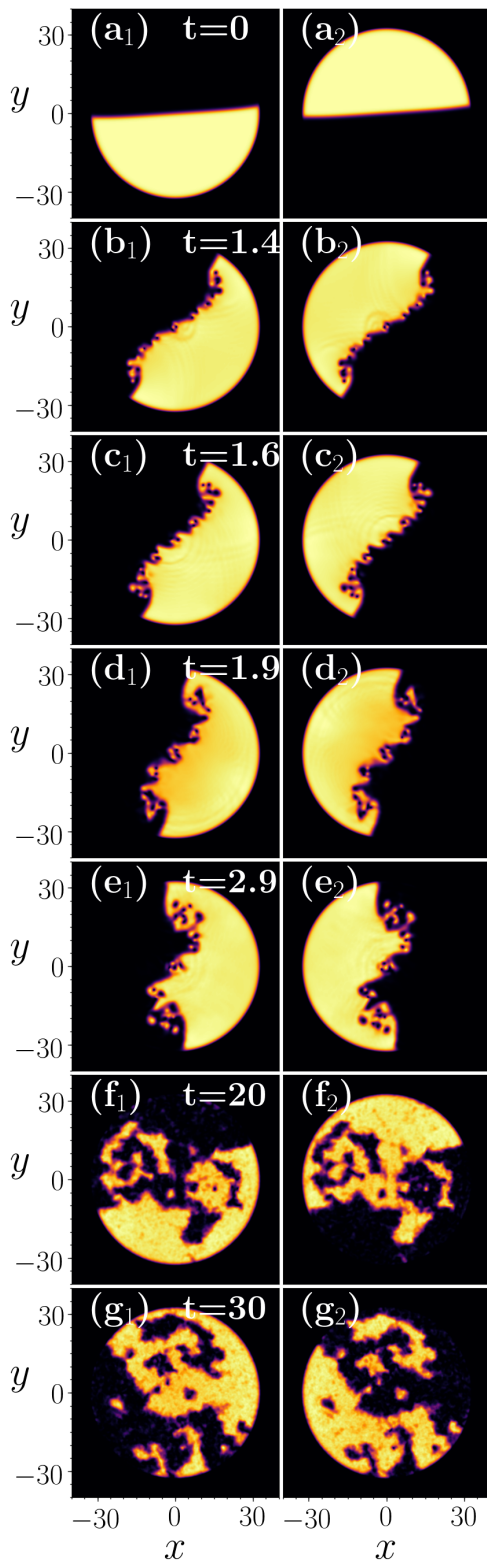


FIG. 4. KH instability in the binary mixture  $^{85}\text{Rb}$  [panels (a<sub>1</sub>)-(g<sub>1</sub>)] and  $^{87}\text{Rb}$  [panels (a<sub>2</sub>)-(g<sub>2</sub>)], showing the respective densities  $|\psi_i|^2$  at different time snapshots (indicated in the left panels), for the immiscible condition  $\delta = 1.05$ . Here, a constant linear force  $\nu_i = (-)^{i+1}0.7$  (in the  $x$ -direction) is applied to the components. The units for time and length are, respectively,  $\omega_{\perp}^{-1}$  and  $l_{\perp}$ . (The full dynamics of this figure is available among the supplemental material.)

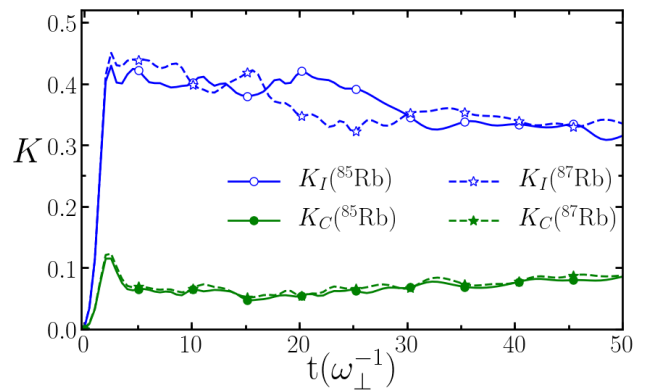


FIG. 5. (Color online) Time evolution of the incompressible (empty symbols) and compressible (filled symbols) kinetic energies  $K$  (units  $\hbar\omega_{\perp}$ ) of the two components, evidencing KH instabilities. The incompressible results become larger than the compressible ones due to the dominance of vortex emission with their interaction. As legends indicate, the solid lines are for  $^{85}\text{Rb}$ , with dashed ones for  $^{87}\text{Rb}$  results.

## B. Kelvin-Helmholtz instability in coupled BECs

The KH instability occurs due to velocity differences across the interface in the classical two-fluid system. KH instability significantly influences the topology of the interface between different-density fluids. This can be developed by introducing a velocity difference between the immiscible mixtures. On quantum KH instability, some recent experiments and analyses were reported in Ref. [81]. In our present numerical simulations for the onset of KH instability, we are assuming the phase-separated  $^{85}\text{Rb}$ - $^{87}\text{Rb}$  BEC mixture. The ground state is prepared as in the case we have used for RT instability [See, panels (a<sub>i</sub>) in Fig. 4], such that it will help us to analyze the main differences in both dynamics. To introduce a velocity difference between the species across the interface, a linear constant force with  $\nu_1 = 0.7$  is applied to the first component,  $^{85}\text{Rb}$ , with a correspondent force  $\nu_2 = -0.7$  applied to the second component,  $^{87}\text{Rb}$ . The introduced instability can be observed in Fig. 4 by a series of panels for the coupled mixture along the time evolution. One should notice, at  $t = 1.4$ , the fluid motion going to the right in (b<sub>1</sub>); and to the left in (b<sub>2</sub>). Due to the immiscibility, together with the radial confinement, the applied velocities to the components induce a rotation in the coupled densities, as time evolves. Roll-up structures forming vortices can be observed, which are generated as producing vortices with the same signs. This vortex production can be detected by using a package for vortex distribution studies, available in [85]. The vortex production and distribution are maintained in the evolution for times much longer than in the case of RT instability, as noticed by comparing Figs. 4 and 1. In this respect, the different dynamics observed for the RT and KH instabilities can be examined from the respective evolutions of the incompressible and compressible kinetic

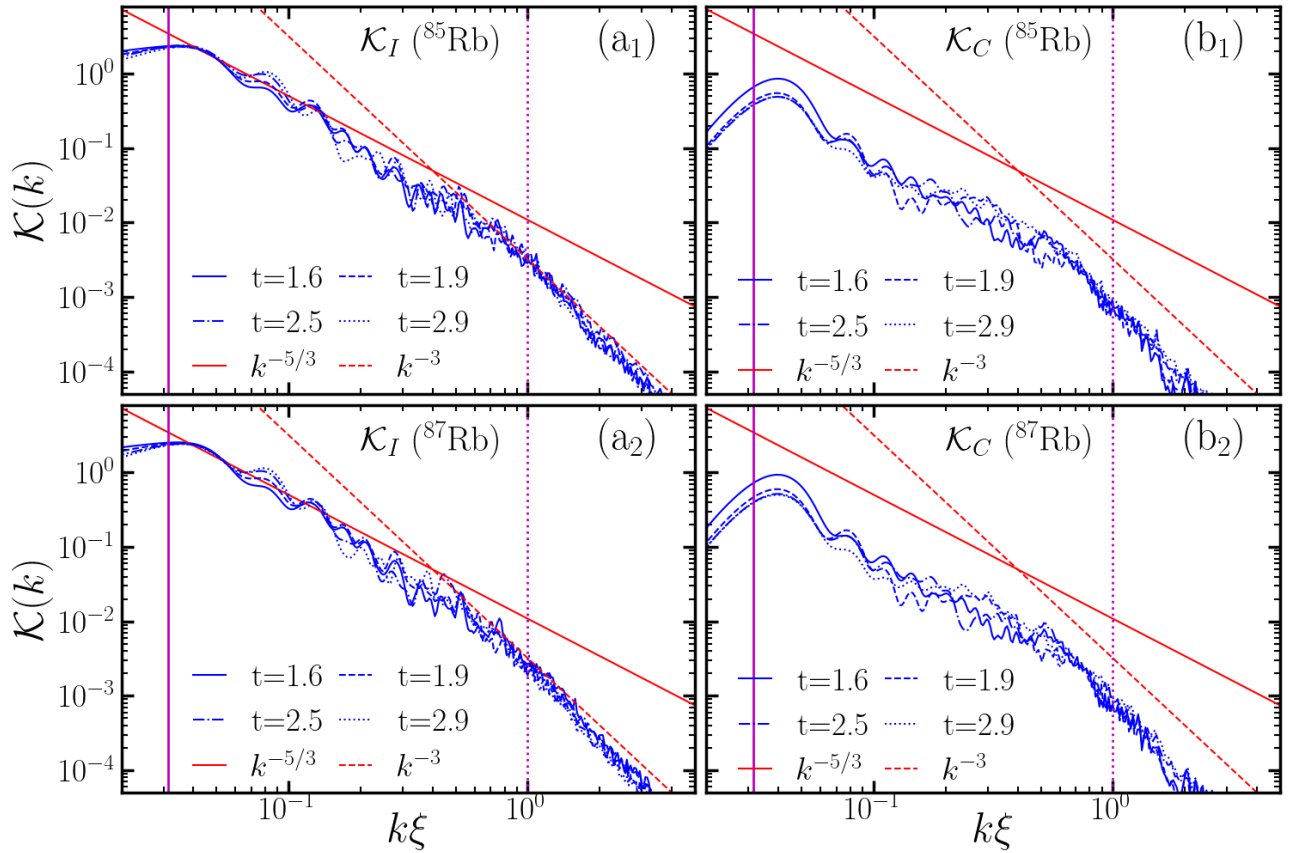


FIG. 6. (Color online) Related to the KH instability represented in Figs. 4 and 5, it is shown the incompressible [panels (a<sub>i</sub>)] and compressible [panels (b<sub>i</sub>)] kinetic energy spectra,  $\mathcal{K}(k)$  (units of  $\hbar\omega_{\perp}l_{\perp}$ ), as functions of  $k\xi$  for the first ( $^{85}\text{Rb}$ ) (upper panels) and second ( $^{87}\text{Rb}$ ) (lower panels) components of the mixture, considering four different instant times  $t$  in the evolution (as indicated inside the panels). The line conventions, units, and definitions follow the same as given in the caption of Fig 3.

energies. In the case of KH instability, corresponding to Fig. 4, Fig. 5 shows that the vorticity dominates all the evolution dynamics, with the incompressible kinetic energies for both components, being more than three times larger than the corresponding compressible kinetic energies (which are related to sound wave propagations). The KH dynamics is quite different from the one observed for RT instability. In the case of RT instability, the vorticity dominance occurs only for  $t < 11$ . This behavior relies on the fact that the constant perturbation is initially introduced along the surface separating the immiscible fluid, which makes both components to move to opposite borders of the trap. As the forces continue acting in such immiscible coupled fluid, one of the immiscible components tries to occupy spaces not occupied by the other component in an almost permanent movement.

Also in this case, as related to the KH instability dynamics shown in Figs. 4 and 5, to help us look for similarities with corresponding classical behaviors for turbulence, we have the Fig. 6 with the corresponding results for the incompressible (left panels) and compressible (right panels) kinetic energy spectra over the wave number  $k$ . As shown, both elements, in this case, have quite similar spectral distributions (incompressible and

compressible), as functions of  $k\xi < 1$ , practically not varying as time evolves along the period of instabilities, represented four instant times,  $t = 1.6, 1.9, 2.5$ , and  $2.9\omega_{\perp}^{-1}$ , as indicated. In the ultraviolet region, the results follow more consistently the  $k^{-3}$  behavior, noticed for ( $k\xi > 0.5$ ). However, for  $k_L < k < 1/\xi$ , the expected Kolmogorov behavior,  $k^{-5/3}$ , is observed more closely in case of compressible energies, with the incompressible kinetic energy behavior being closer to  $k^{-2}$ , with the cascade behavior changing starting near  $k\xi \approx 0.5$ . It is known that the compressible energy spectrum may follow a Kolmogorov-like scaling  $k^{-5/3}$  if it is strongly coupled to the incompressible one [8, 20]. In Fig. 6, this is observed in the KH instability results, clarifying that no strong density oscillations and other compressible effects deviate from the expected behavior. Also, in this case, the similar scalings for both incompressible and compressible modes indicate that the external forces are exciting equally such modes. Comparatively, we can see a different behavior in the compressible kinetic energy of RT, shown in Fig. 3, in which stronger oscillations are observed at all different instability instants that we have selected. The expected turbulent-like behavior is quite restricted in time, for the RT instabilities, mainly due to

the strong dominance of compressible effects, as shown in Fig. 2 and panels (b<sub>i</sub>) of Fig. 3.

### The RT and KH instabilities and the miscibility

As concluding the analysis of the RT and KH instabilities, discussed in the above A and B subsections, with Fig. 7 we are verifying how the initial immiscibility regime of the mixture behaves along the time evolution, by considering the density overlap parameter  $\Lambda$  defined by Eq. (6). As observed, because the interspecies and intraspecies are kept the same along the process of evolution, the mixture remains almost immiscible, besides the attractive force applied between the two species, which makes both components of the mixture share regions that are overlapping. In the case when we have RT instability, there is a tendency for the system to become more miscible during the time interval when the main instability is being observed, with a maximum for  $\Lambda$  near  $t = 9$  (close to the time instant when compressible effects, leading to stronger density oscillations, start dominating the dynamics, as seen in Fig. 2). Still, the overlap represented by  $\Lambda$  remains below 20%, next decreasing below 2% in the long-time evolution. For the case, we have KH instability, with the density evolution of the mixture represented by Fig. 4,  $\Lambda$  increases slightly from zero and becomes stable near 3% for longer-time simulations. Therefore, the Fig. 7 results show that, for both RT and KH cases produced by the linear-force perturbation, there are no immiscible to miscible transitions. The tendency of the RT instability to become more miscible occurs only in a shorter time interval when one can notice a transition in the kinetic energy spectrum, from incompressible to compressible kinetic energy dominance.

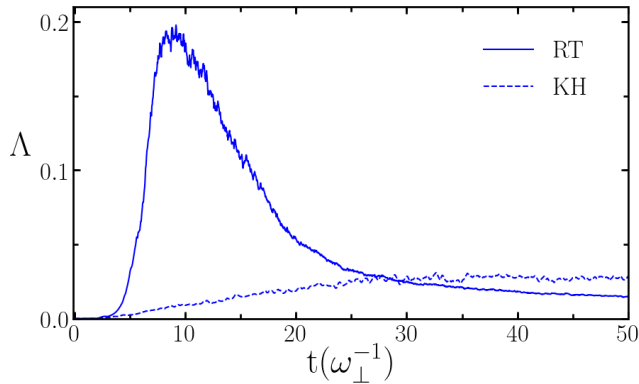


FIG. 7. Time evolution of  $\Lambda$  (dimensionless) [Eq. (6)], representing the density overlaps for the RT (solid line) and KH (dashed line) instabilities in the  $^{85}\text{Rb}$ - $^{87}\text{Rb}$  mixture. Respectively, the density evolutions are in Figs. 1 and 4).

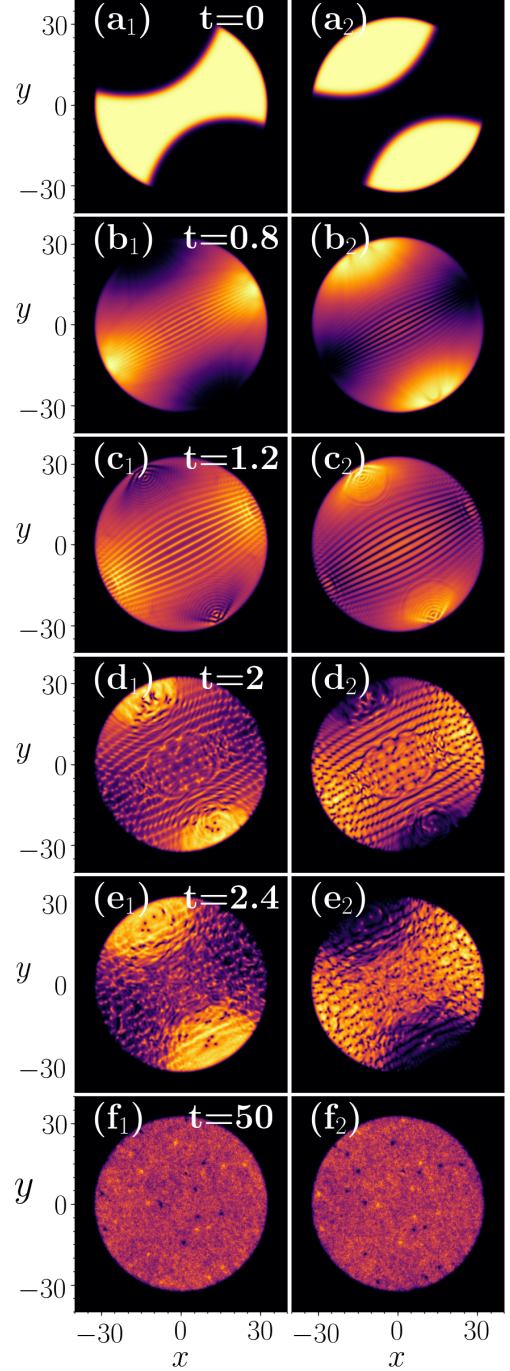


FIG. 8. IMQT instability is shown through the evolution of the densities, for the  $^{85}\text{Rb}$ - $^{87}\text{Rb}$  mixture, with the ground state prepared in an immiscible regime (with  $\delta = 1.02$ ) in a projected “tennis-ball” shape configuration at  $t = 0$ , with the  $^{85}\text{Rb}$  centrally located [shown in (a<sub>1</sub>)] and  $^{87}\text{Rb}$  in the remaining trap confinement [shown in (a<sub>2</sub>)]. The evolution starts with a sudden reduction of  $a_{12}$  to  $75a_0$  ( $\delta = 0.75$ ), which remains along the dynamics. The snapshot instants  $t$  are given inside the left panels. The units for time and length are, respectively,  $\omega_{\perp}^{-1}$  and  $l_{\perp}$ . (The full dynamics of this figure is available among the supplemental material.)

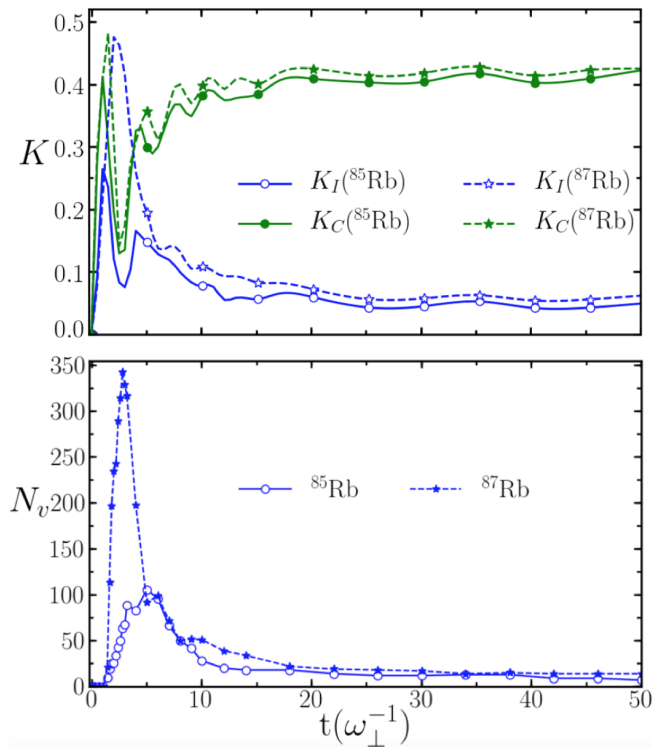


FIG. 9. (Color online) For the IMQT instability given in Fig. 8, with the first species,  $^{85}\text{Rb}$ , initially, at the central part, it is shown the time evolutions of the compressible and incompressible kinetic energies  $K$  (units  $\hbar\omega_{\perp}$ ) (upper frame) and the corresponding number of vortices  $N_v$  (lower frame), with convention as indicated inside the frames.

### C. Immiscible to miscible quenching transition instability in coupled BECs

The following simulations with the binary  $^{85}\text{Rb}$ - $^{87}\text{Rb}$  mixture consider the dynamical IMQT instability by preparing the original coupled system in an immiscible condition ( $\delta > 1$ ), with the interspecies two-body interaction larger than the intraspecies one,  $a_{12} > a_{ii}$  (also here,  $a_{11} = a_{22}$ ). Different from our simulations for RT and KH instabilities, here we are not applying linear perturbations to obtain the dynamical evolution. Instead, a quench-induced transition is applied by introducing a sudden reduction in the two-body interspecies scattering length, such that the coupled system moves from immiscible ( $\delta > 1$ ) to miscible ( $\delta < 1$ ) conditions. The motivation for studying the dynamic behavior of cases where instability arises from nonlinear interactions is to compare it with the previous studies in which the onset of instabilities was carried out through external forces. Therefore, we apply the same approach as before. Here, we find it appropriate to probe two different initial immiscible 2D spatial configurations for the ground state, as follows: (i) First, with *tennis-ball projected format*, with one species at the central part, identified as “central”; (ii) Second, with *axial format* with both species side-by-side,

identified as “axial”.

### IMQT with “tennis-ball” shaped initial state

The first initial configuration considered in our study of IMQT instability is by having the two species within a tennis-ball 2D projected shape, within a three-sliced initial configuration, having the  $^{85}\text{Rb}$  in the central part, with the other species,  $^{87}\text{Rb}$ , located at both sides of the centrally localized component, as shown in panels ( $a_1$ ) and ( $a_2$ ) of Fig. 8. The quench-induced interaction is introduced by a sudden reduction of  $a_{12}$ , such that the miscibility of the mixture goes from  $\delta = 1.02$  (with  $a_{12} = 102a_0$ ,  $a_{ii} = 100a_0$ ) to  $\delta = 0.75$  (with  $a_{12} = 75a_0$ ) [86]. Given the initial configuration and quenching, the miscibility starts to occur from both sides of the centrally located component, at the two spacial borders shared by the two species. The dynamics can be followed through the snapshots ( $a_i$ ) to ( $f_i$ ) for the time evolution of the densities, shown in Fig. 8. The corresponding kinetic energy evolutions, with the associated vortex dynamics, and spectral analyses follow, respectively, through Figs. 9 and 10.

Interesting instability dynamics can be observed in the overlap of both densities, in the initial transient period till  $t \approx 2.4$  [as shown in the panels ( $b_i$ ) to ( $e_i$ ) of Fig. 8], when going from the immiscible to a miscible configuration, with nonlinear interference patterns being noticed. Similar to the ones experimentally observed in Ref. [87] for the interference of two Bose condensates, these patterns are attributed to the difference between initial and final miscibility factor  $\delta$ , which in this case corresponds to a quenching reduction of the repulsive interspecies parameter  $a_{12}$  of about  $27a_0$ . The connection between the observed interferences obtained in the GP mean-field theory with dark solitons (which can be generated for repulsive nonlinear interactions) was discussed in Ref. [88]. The interference patterns noticed in Fig. 8 resembles planar dark solitons in propagation through the binary mixture. Among several related studies of dark solitons in BEC we can mention the Refs. [89–91]. Planar dark solitons are subject to snake instability, where the dark solitons decay into dipolar vortices [92]. These vortex dipoles are indeed observed in our simulation. The particular geometric form of the interference fringes generated in the evolution of the miscibility also occurs due to the initial condition of the prepared immiscible coupled states, with  $^{87}\text{Rb}$  fragmented in two distinct regions. With the sudden reduction in the interspecies repulsive interaction, the  $^{87}\text{Rb}$  atoms species move towards the center from both sides, interacting with the  $^{85}\text{Rb}$  located in the central region, as seen in the panels ( $c_i$ ) of Fig. 8. Plenty of vortex dipoles and sound waves (phonon excitations) are produced in both densities, as one can observe in the corresponding time evolution, which are supported by the results shown in Fig. 9 for the incompressible (related to vorticity) and compressible (related to sound



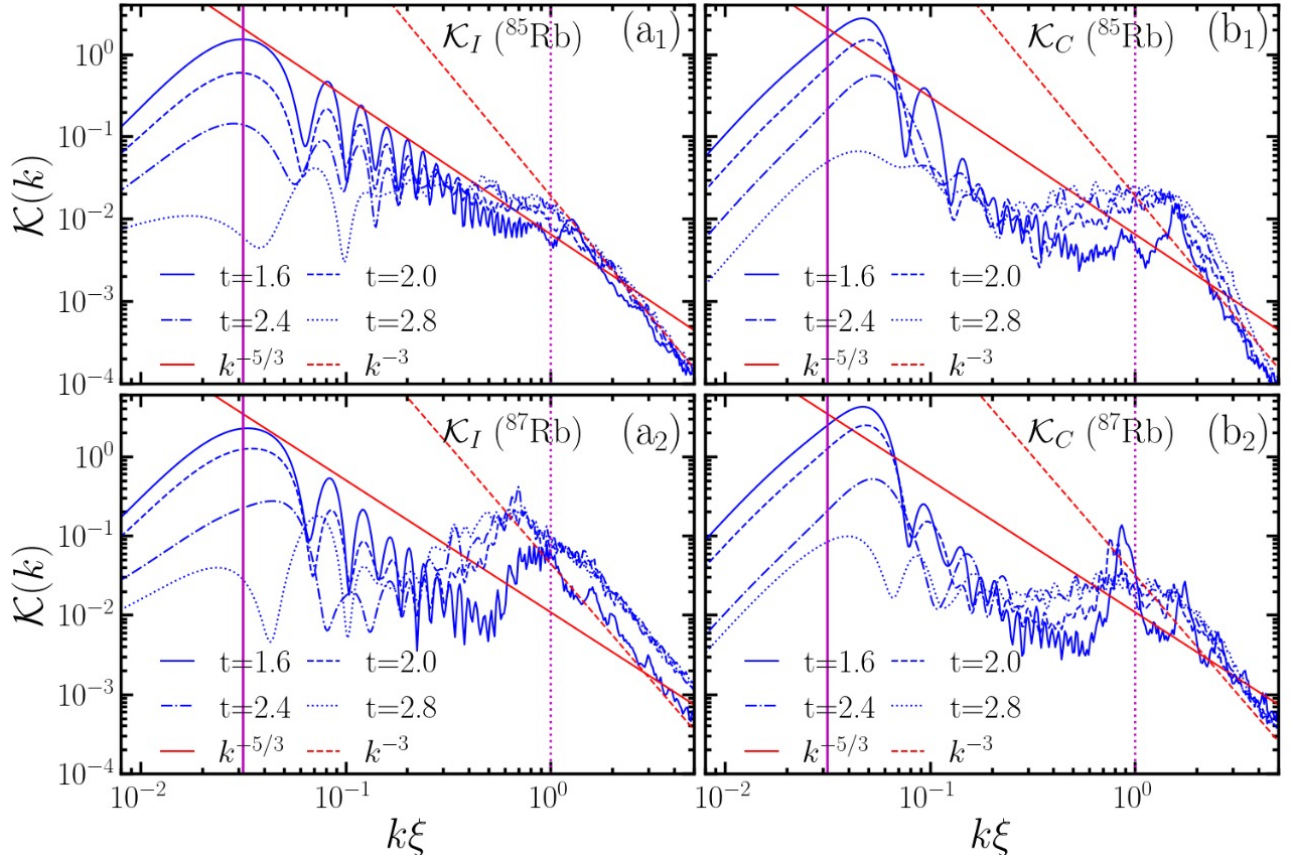


FIG. 10. (Color online) Related to the IMQT instability represented in Figs. 8 and 9, it is shown the incompressible [panels (a<sub>i</sub>)] and compressible [panels (b<sub>i</sub>)] kinetic energy spectra,  $\mathcal{K}(k)$  (units of  $\hbar\omega_{\perp}l_{\perp}$ ), as functions of  $k\xi$  for the first ( $^{85}\text{Rb}$ ) (upper panels) and second ( $^{87}\text{Rb}$ ) (lower panels) components of the mixture, considering four different instant times  $t$  in the evolution (as indicated inside the panels). The line conventions, units, and definitions follow the same as given in the caption of Fig 3.

waves) parts of the kinetic energy spectrum. The vortices are spontaneously generated when the components are interacting, leading to annihilations and sound wave productions. As noticed from the two panels of Fig. 9 there is a close relation between the incompressible part of the kinetic energy with the vortex numbers  $N_v$ , in the evolution of the mixture, with the peaks of  $N_v$  slightly shifted to the right of the corresponding peaks observed for the  $K_{i,I}$  ( $i = ^{85}\text{Rb}, ^{87}\text{Rb}$ ). As also expected, the initial production of vortices is much larger inside the element density which was initially located outside the center, such that the larger peaks are observed in  $K_{i,I}$  and  $N_v$  for  $^{87}\text{Rb}$ .

In the long-time evolution of the mixture, we notice that sound-wave propagations due to phonon excitations become dominant, as noticed in the upper panel of Fig. 9.  $K_{i,I}$  and  $N_v$ , representing the vorticity of both species, decrease to more or less permanent stable limits. In this asymptotic limit, one can follow the dynamics of the vortex propagation inside the coupled fluid. The particular vortices observed in the densities of one of the components can be followed in the numerical simulations, which are represented by holes in movement inside the density profile. Correspondingly, one can observe a density in-

crease of the other species at the same positions, implying one component filling the spatial holes opened by the other component inside the trap. Such long-time dynamics can still be distinguished in both coupled fluids since they are still in a condition not fully miscible, with  $\delta = 0.75$ . This will be further discussed, considering the asymptotic incomplete overlap  $\Lambda$  of the densities.

The spectral behavior of the incompressible and compressible kinetic energies, respectively given by  $\mathcal{K}_I(k)$  and  $\mathcal{K}_C(k)$ , can be analyzed through the results shown in Fig. 10 for the two components, in which the turbulent dynamics are being identified in the initial period of the evolution by considering four instants. As noticed, the classical Kolmogorov  $k^{-5/3}$  can be evidenced approximately for  $k\xi < 0.5$  (by averaging the oscillations) only at some particular time interval close to  $t \approx 1.6$ , being more clear in case of incompressible kinetic energies. In the ultraviolet region, the  $k^{-3}$  behavior can also be approximately distinguished at a short time interval  $t < 2.8$ . For all selected time instants of the dynamics, shown in this Fig. 10, it is also possible to notice transient energy increases (incompressible and compressible) occurring in an intermediate  $k$  interval, starting near  $k\xi \approx 0.8$ , when the  $\mathcal{K}_{i,I}(k)$  and  $\mathcal{K}_{i,C}(k)$  behaviors are expected to

change from  $k^{-5/3}$  to  $k^{-3}$ . This kind of effect is deviating from the expected Kolmogorov's cascade transition in the energy spectra. It is interpreted as due to nonlinear dynamical interactions at intermediate scales, with energies temporarily accumulated before being fully transferred between the scales. It is being recognized as similar to the quantum superfluid "bottleneck effect", at which energy piles up at scales just before the dissipation range [93, 94]. Often seen in 3D turbulence, it can also occur in 2D or quasi-2D systems. The bottleneck effect arises due to a mismatch between the energy transfer rate and the dissipation rate at small scales. Within the perspective of further studies, it is also noticed that such bottleneck effect is more pronounced for the element not initially at the center.

### IMQT with axial shaped initial state

The other initial configuration that we consider for the IMQT instability is represented by both immiscible densities located side-by-side, as shown in panels (a<sub>1</sub>) and (a<sub>2</sub>) of Fig. 11, with the time evolution represented by the other panels of this figure. In this case, the ground state is initially prepared with  $a_{12} = 105a_0$  ( $\delta = 1.05$ ). The corresponding kinetic energy analysis and number of vortices detected are shown in Fig. 12. As in the case with the species 1 centrally located, in the present case the sudden quenching of  $a_{12}$  will be to  $a_{12} = 75a_0$ , such that we will have  $\delta = 0.75$  along the dynamical evolution. As shown, the final miscible configuration is similar in both cases, as shown in the respective panels (f<sub>i</sub>) of both Figs. 8 and 11. However, the dynamical process noticed in Fig. 8, in the same initial time interval of instabilities, because in the spatial configuration of Fig. 11 both species are symmetrically occupying the space in the trap region.

Considering the kinetic energy, together with vortex dynamics results, respectively shown in the two panels of Fig. 12, a similar behavior can be observed as the ones shown in Fig. 9 in the long time evolution, with the dominance of the compressible modes. The main difference occurs in the initial evolution,  $t \lesssim 6$ . Given the symmetric spatial distribution at  $t = 0$ , the  $K_{i,I}$  and  $N_v$  peaks associated with the vorticities are located at the same time position for both components. Again, the peaks for  $N_v$  are slightly shifted as related to the  $K_{i,I}$  peaks, implying the vortex dynamics following the incompressible kinetic energy behavior. In the long-time interval, with the condensate mixture searching for miscible configuration equilibrium, the number of vortices of both components reduces to about the same number below 20. In this long time interval, with both parts of the kinetic energy converging to different asymptotic limits the incompressible kinetic energy is reduced to less than 1/8 of the compressible part, reflecting the dominance of density fluctuations and sound-wave productions, with reduced vortex dynamics, as one can better appreciate in the cor-

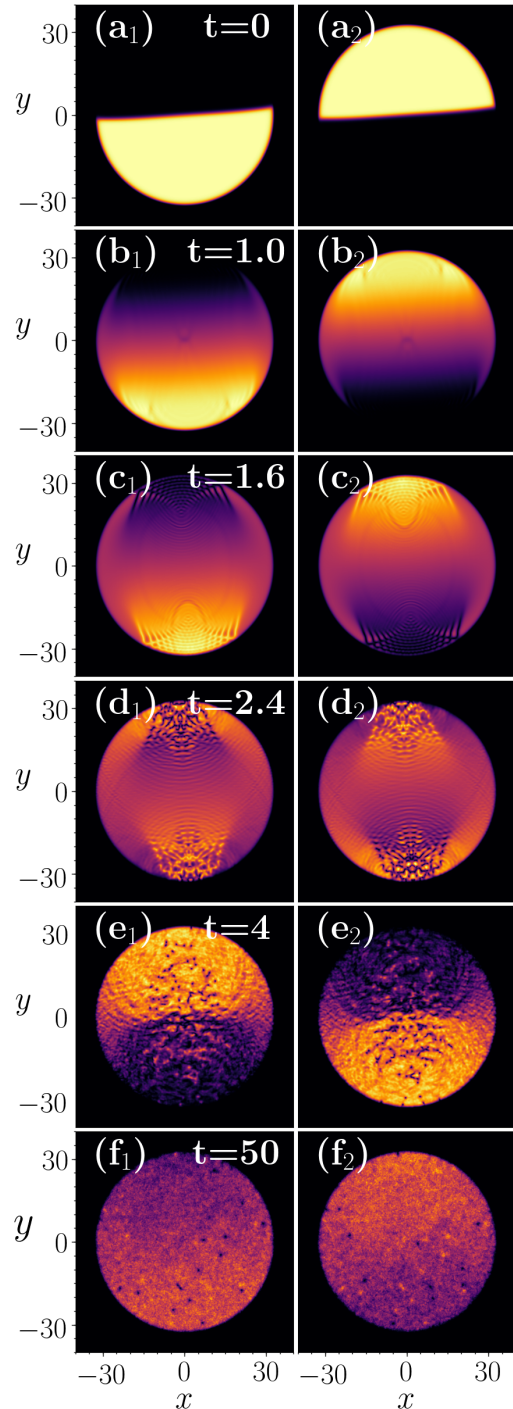


FIG. 11. IMQT instability is shown through the evolution of the densities, for the  $^{85}\text{Rb}$ - $^{87}\text{Rb}$  mixture, with the ground state prepared in an immiscible regime (with  $\delta = 1.05$ ) in an axial geometrical configuration at  $t = 0$ , with  $^{85}\text{Rb}$  located in the lower part [shown in (a<sub>1</sub>)] and  $^{87}\text{Rb}$  in the upper part [shown in (a<sub>2</sub>)]. The evolution starts with a sudden reduction of  $a_{12}$  to  $75a_0$  ( $\delta = 0.75$ ), which remains along the dynamics, as shown from (a<sub>i</sub>) till (f<sub>i</sub>). The snapshot instants  $t$  are given inside the left panels. The units for time and length are, respectively,  $\omega_{\perp}^{-1}$  and  $l_{\perp}$ . (The full dynamics of this figure is available among the supplemental material.)

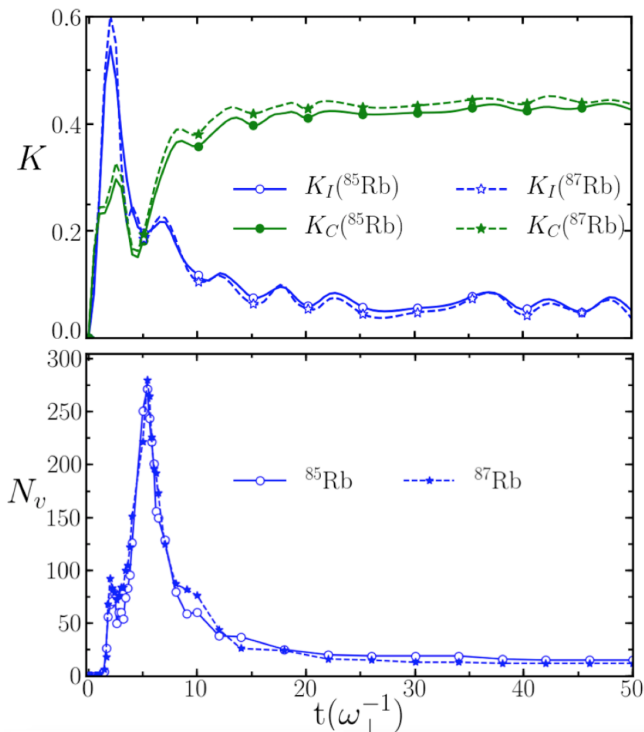


FIG. 12. (Color online) For the IMQT instability given in Fig. 11 with axial initially separated elements,  $^{85}\text{Rb}$  (solid lines) and  $^{87}\text{Rb}$  (dashed lines), the above results are for the time evolutions of the kinetic energies  $K$  (units  $\hbar\omega_{\perp}$ ) (upper frame) and the corresponding number of vortices  $N_v$  (lower frame), with convention as indicated inside the frames.

responding animations (See supplementary material).

In the four panels of Fig. 13 we are showing the results for the incompressible and compressible kinetic energy spectra over the product of the wave number  $k$  with the healing length  $\xi$ . Quite illustrative of the common behavior of the two components of the mixture, when they start with similar space configurations, in their initial condition [see panels (a<sub>i</sub>) of Fig. 11], are the results observed in the spontaneous production of vortices, shown in Fig. 12. In this case, the small mass difference between the species only appears in the long time interval, with the smaller-mass component,  $^{85}\text{Rb}$ , corresponding to a slightly greater number of vortices than the ones generated in the  $^{87}\text{Rb}$ . These results follow the ones obtained by the incompressible and compressible modes of the kinetic energy observed in Fig. 12, in which in the long-time interval we have more production of sound waves, within a behavior similar to the case of the density distribution evolution of Fig. 8, which was discussed before.

When in the initial condition we have the light element located in the sliced central part (seen in Fig. 8), the time evolution of the spectrum (shown by the  $k$  behavior in Fig. 10) presents fluctuations stronger than the corresponding case, Fig. 11, with elements axially located at  $t = 0$ . In Fig. 10, the  $k^{-5/3}$  behavior can be observed in the incompressible spectrum only at some particular time

of the instability, with the compressible modes related to sound waves having stronger and nonuniform behavior, which apparently affects the incompressible mode. As related to Fig. 11, with axial spacial configuration, the spectrum shown by Fig. 13 becomes quite stable in the interval  $k\xi < 1$ , as time evolves. For both species, the approximate  $k^{-5/3}$  behavior is noticed in the interval  $k\xi < 1$ , besides the fact that the cascade behavior to  $k^{-3}$  be not clearly characterized for  $k\xi > 1$ . The strongest changes in the dynamical behavior of the spectrum, observed in Fig. 10, can be attributed to the fact that the two densities in the miscible dynamical process have the atomic interspecies interactions happening in two region borders near the center of the trap. In the axially separated case, shown in Fig. 11, the dynamics is mainly dictated by the interspecies interactions starting in just one border separation between the species, in a more symmetric form.

Similarly to the case discussed for Fig 10, in the results presented in Fig 13 it is also noticed transient energy increases (both incompressible and compressible) occurring in an intermediate range  $k$ , starting near  $k\xi \approx 0.8$ . As already discussed, the effect is being recognized as similar to the “bottleneck effect” [93, 94]. Since both cases are related to sudden nonlinear changes in the interactions, such an effect confirms that it should be interpreted as due to nonlinear dynamical interactions at intermediate scales, with the energies temporarily accumulated before being fully transferred across the scales.

### The IMQT instabilities and the miscibility

For these two cases of IMQT instabilities, the real-time propagation of the overlap between the two densities is provided by the time dependence of  $\Lambda$  [given in (6)], with the results displayed in Fig. 14.  $\Lambda$  shows how dynamically the miscibility evolves, when the two-body interspecies is suddenly reduced, such that  $\delta$  goes from 1.02 to 0.75 in case of the coupled densities are represented by Fig. 8; and goes from 1.05 to 0.75 in case they are represented by Fig. 11. The effect of the initial conditions in the long-time evolution can better be appreciated by the results shown in Fig. 14, as indicating how the two kinds of mixtures go dynamically from immiscible to miscible configurations due to the sudden changes in the value of  $\delta$ . In the first time interval,  $t < 10$ , the differences are recognized as due to the distinct spatial configurations when the sudden reduction was applied to the interspecies interaction. In the other extreme, asymptotically, for both cases, the averaging values of the time evolutions of  $\Lambda$  converge consistently to about the same value near 0.8, which is quite close to 0.75, the final quenched value of  $\delta$ . Such behavior, as well as the results obtained in both simulations shown in Figs. 8 and 11, are indicating that in the asymptotic limit what remains from the initial conditions are the averaged value of  $\Lambda$  (close to 0.8 for both cases) and the oscillating be-



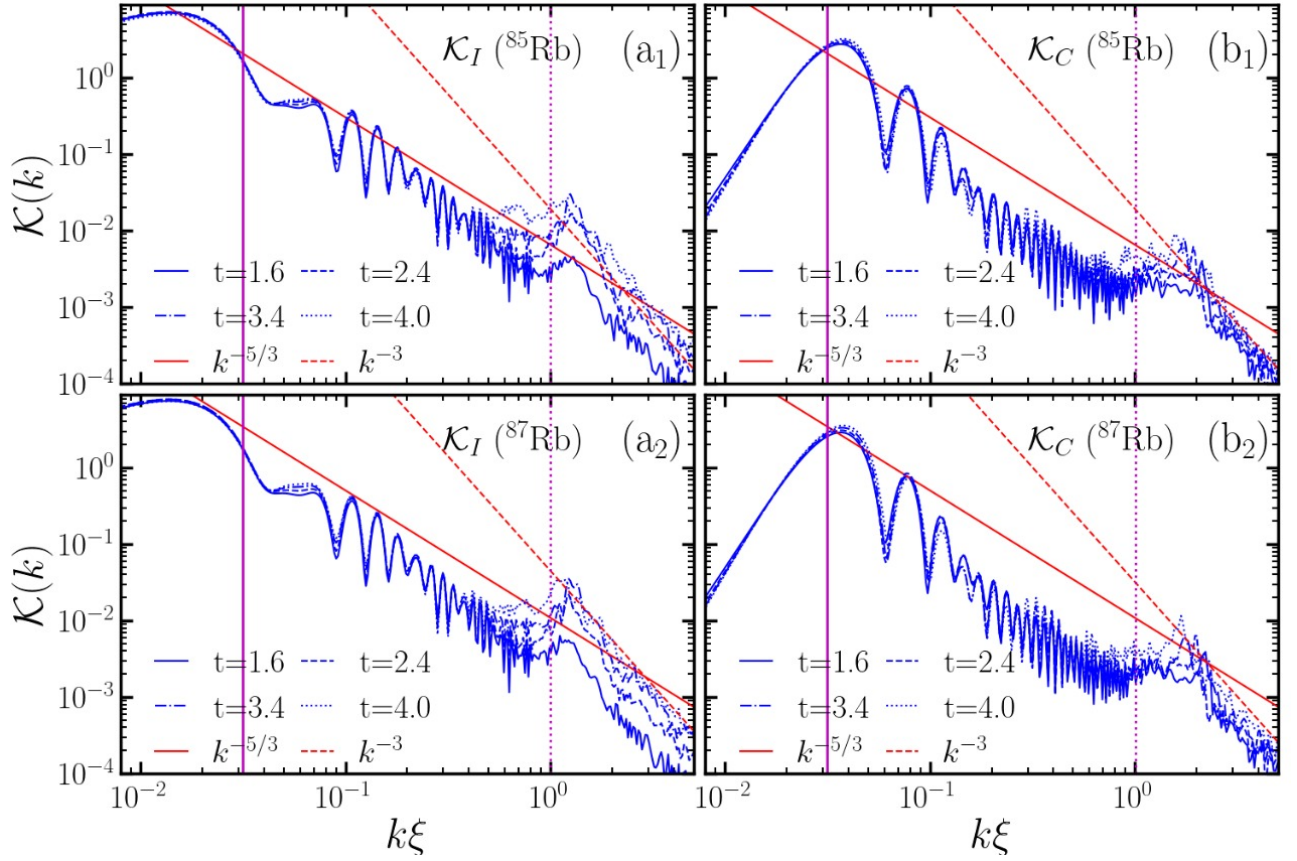


FIG. 13. (Color online) Related to the IMQT results given in Figs. 11 and 12, the incompressible [panels (a<sub>i</sub>)] and compressible [panels (b<sub>i</sub>)] kinetic energy spectra,  $\mathcal{K}(k)$  (units of  $\hbar\omega_{\perp}l_{\perp}$ ), are shown as functions of  $k\xi$  for the first ( $^{85}\text{Rb}$ ) (upper panels) and second ( $^{87}\text{Rb}$ ) (lower panels) components of the mixture, considering four different instant times  $t$  in the evolution (as indicated inside the panels). For comparison with the results, shown by the inclined straight lines, we have the classical power-law behaviors,  $k^{-5/3}$  and  $k^{-3}$ . With the healing lengths (both components) being  $\xi \sim 0.4l_{\perp}$ ,  $k$  is given in units of  $l_{\perp}$ .

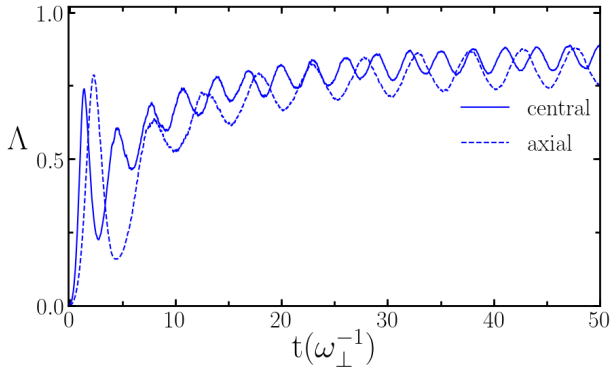


FIG. 14. Time evolution of  $\Lambda$  (dimensionless) [Eq. (6)], representing the density overlaps for the IMQT instabilities, with central (solid line) and axial (dashed line) initially space separated  $^{85}\text{Rb}$  and  $^{87}\text{Rb}$  components. Respectively, the density evolutions are shown in Figs. 8 and 11).

haviors. Apparently, from the results of Figs. 8 and 11, for  $t > 20$ , the vortex dynamics are very similar in both cases, such that the initial spatial configurations have

limited relevance (if any) for the behavior in the asymptotic limit. However, a striking difference between the two cases occurs in the different oscillating cycles of the miscibility overlap  $\Lambda$ , which we interpret as reflecting the initial sudden change of  $\delta$ . In the first case, with initial three sliced regions, named *central* (considering that the species 1 is at the central slice), the  $\delta$  quenching varies from 1.02 to 0.75, such that  $\Delta\delta_C = 0.27$ , whereas in the second case, when the confining region was split into two parts,  $\Delta\delta_A = 0.30$ . The central case implies a slightly faster transition, which results in a larger frequency (and smaller amplitude) than the second case. Another point to consider is that, with the initial configuration given by Fig. 8, the main region for the interspecies interaction and possible interferences is located at the central part [see panels (c<sub>i</sub>) and (d<sub>i</sub>) of Fig. 8]. In the case of Fig. 11, the interactions occur symmetrically on both sides, with densities increasingly closer to the trap limits, where one can verify the main interference patterns [see panels (c<sub>i</sub>) and (d<sub>i</sub>) of Fig. 11]. By a close observation of Fig. 14, one should note that in the same time interval between  $t = 20$  and  $t = 50$ , we have 10 oscillations in case of central initial configuration, against 6 oscillations in the



case of axial configuration, such that we can extract the asymptotic ratio limit between the oscillating frequencies of  $\Lambda$ , which is given by  $\mathcal{R}_\Lambda \approx 5/3$  (5 cycles of the central case corresponding to 3 cycles of the axial case). By looking for a relation between the asymptotic oscillating frequencies with the initial quenching condition, we can observe that such oscillation may be induced by the quenching differences, which is  $\Delta\delta_A = 0.30$  for the axial case, and  $\Delta\delta_C = 0.27$  for the central case. The ratio of these two quantities,  $\Delta\delta_A/\Delta\delta_C = 10/9$ , turns out to be identical to  $(2/3)\mathcal{R}_\Lambda$ . This may be a curious coincidence when considering that, initially, the central case has three regions for interspecies interactions, whereas the axial case has only two regions. Indeed, it looks like an interesting topic for further investigations to consider long-time evolutions of binary mixtures under different time-dependent transitions from immiscible to miscible regimes. To this aim, a time-dependent interspecies scattering length could be assumed as in Ref. [95] to study possible resonant patterns in the BEC mixture.

#### IV. CONCLUSIONS AND SUMMARY

In this work, we have systematically investigated three distinct types of instabilities, each with its unique characteristics and underlying mechanisms. The onsets of Rayleigh-Taylor (RT) and Kelvin-Helmholtz (KH) instabilities are driven by linear perturbations, consistent with their classical counterparts. In contrast, the immiscible-to-miscible quenching transition (IMQT) instabilities arise from nonlinearity changes, triggered by sudden reductions in the two-body interspecies scattering length  $a_{12}$ . These IMQT instabilities were explored under two distinct initial conditions, highlighting the critical role of nonlinear dynamics in their evolution. All numerical simulations were conducted for coupled condensates initially confined in a uniform 2D circular box, prepared in immiscible configurations. Our findings not only deepen the understanding of these instabilities in quantum systems but also provide a foundation for further exploration of nonlinear phenomena in multi-component Bose-Einstein condensates. Results of this study suggest dedicated investigations for each kind of instability, by exploring extensions to more complex geometries, different initial conditions, or by looking for new insights into the interplay between linear and nonlinear instabilities in quantum fluids.

**RT Instability:** Within an immiscible state, kept constant by  $\delta = 1.05$ , with both species axially separated, this instability is initiated by an oscillatory perturbation applied to one of the components for  $t \leq 2$ . Subsequently, constant forces are applied to both species, perpendicularly to the border interface between the species, in opposite directions throughout the process, driving the development of the instability. The combination of the initial perturbation and the opposing forces leads to the charac-

teristic interpenetration and mixing patterns associated with the RT instability, highlighting the role of competing forces in destabilizing the system.

With the main results provided in Figs. 1-3, the onset of RT instability presents a striking similarity with standard results obtained with a mixture of two classical immiscible fluids subject to attractive forces between them. As shown in Fig. 2 by the analyses of the incompressible and compressible parts of the kinetic energy, the vorticity dominates the dynamics during the first stage of time evolution, till  $t \approx 10\omega_\perp^{-1}$ , with plenty of vortex-antivortex production in the interval  $4 < t < 10$ . For longer-time evolution, sound-wave production starts dominating the dynamics, with part of kinetic energy being transferred from incompressible to compressible. However, the vorticity remains high enough within the mixture (further observed in comparison to other cases we have studied). The dynamical overlap of the densities  $\Lambda$  (shown in Fig. 9), reflects the applied immiscible condition. The coupled system has a small tendency to become more miscible near the time interval when the compressible modes start dominating the dynamics. Our analysis in Fig. 3 of the corresponding spectra shows that for both incompressible and compressible energies, the  $k^{-3}$  behavior can be identified for  $k\xi > 1$ , in the interval  $t \approx 4.1$  to  $6.4\omega_\perp^{-1}$ . However, in the same specific time interval, the classical scaling law  $k^{-5/3}$  expected for turbulence on the intermediate  $k$  region ( $k\xi < 1$ ), can only be identified in case of the incompressible kinetic energy results (dominated by the motion of quantized vortices). In this case, the compressible energies are not being transferred through a cascade process as the incompressible ones, which is understood as due to sound wave radiations and dissipative effects. At large times,  $t > 20\omega_\perp^{-1}$ , as seen in Fig. 2, the compressible and incompressible modes converge to constant values, with the corresponding compressible spectra becoming more flat in the ultraviolet limit. Such results imply approximate equilibrium with no significant energy transfer across scales.

**KH Instability:** With the same initial immiscible condition as in the RT case ( $\delta = 1.05$ ), this instability is generated by applying constant forces to both components in opposite directions. They act parallel to the interface (borderline surface) between the species, creating a velocity shear across the boundary. The resulting velocity differences between the fluids trigger the KH instability, leading to characteristic rolling patterns at the interface. This mechanism highlights the critical role of shear flow in driving interfacial instabilities in coupled condensates.

The main results in this case are given in Figs. 4-6, showing that the KH dynamics is dominated by vorticity along all the time evolution, in contrast with results obtained for the RT dynamics. The two-component spectra over the wave number  $k$  also present a behavior more uniform than the RT instability case during the onset of instability. As shown in Fig. 6 for the kinetic energy spec-

tra of both species, in the ultraviolet limit the expected  $k^{-3}$  behavior is noticed for both compressible and incompressible kinetic energy cases. This behavior starts close to  $k\xi \sim 0.5$ . In the interval  $k_L\xi < k\xi < 0.5$ , the  $k^{-5/3}$  behavior is better observed in the compressible energy modes, deviating to  $\sim k^{-2}$  in the incompressible cases. Essentially, the similar scaling for both incompressible and compressible modes are implying that the specific external forces are equally exciting these modes in the KH instability case, with the constraints homogenizing the energy transfer processes. In the long-time evolution, the vorticity and sound-wave production remain approximately stable, kept by the constant forces.

As related to the evolution of the overlap between the densities, the KH instability differs from the RT instability mainly during the onset of instabilities, as shown in Fig. 7. Along all the KH dynamics,  $\Lambda$  remains below 0.03 (less than 3% miscible).

**IMQT Instability:** Here, the critical role of nonlinearity changes in destabilizing the system is highlighted. The study underscores the interplay between interaction strength and phase separation in coupled condensates. The instability is triggered by quenching the nonlinearity of the system, through a sudden transition from an immiscible to a miscible condition, with the miscible condition kept throughout the dynamics.

Two possible initial immiscible configurations are assumed. The first, with  $\delta = 1.02$ , having the two species occupying three distinct regions inside the trap, in a kind of projected "tennis-ball" configuration, as seen in the  $t = 0$  panels ( $a_i$ ) of Fig. 8. Symmetrically, the  $^{85}\text{Rb}$  is placed in the central part, with  $^{87}\text{Rb}$  split in the other two parts. The second, with  $\delta = 1.05$ , in an axially symmetric configuration, with each species having half of the trapping region, as seen in the  $t = 0$  panels ( $a_i$ ) of Fig. 11. In both cases, the quenching from an immiscible to a miscible system is performed by a sudden change in the interspecies interaction, such that the onset of the dynamics is developed with  $\delta = 0.75$ . As observed in the first case, we have an asymmetric initial production of vortices, with the component located in the center ( $^{85}\text{Rb}$ ) presenting less vorticity than the other component. This is an expected result, considering the sudden change from immiscible to miscible configuration, with the element outside the center,  $^{87}\text{Rb}$ , moving to the central part through two boundary edges between the species, while the element in the center,  $^{85}\text{Rb}$ , remains more confined by the pressure of the second component. In the second case, with the initial configuration having both components symmetrically positioned, similar production of vortices and sound waves are noted throughout the temporal evolution, as seen in Fig. 12 for the incompressible kinetic energy part (upper panel), with the corresponding number of vortices (lower panel). The respective spectra, given in Figs. 10 and 13, show similar behavior for the incompressible and compressible modes, with energy oscillations between the two modes (indi-

cating energy transfer) for both species. When averaging the oscillations, the behaviors of the incompressible mode (for  $k\xi < 0.5$ ) are close to  $k^{-5/3}$  in the first case, as seen in Fig. 10; and deviating slightly towards  $k^{-2}$  in the case shown in Fig. 13. The results also indicate the coupling between the compressible and incompressible modes, as both follow approximately the same behavior.

Characteristic of both IMQT instabilities and distinguishable from RT and KH instabilities, a kind of "bottleneck effect" is noted in the energy spectra [93, 94]. It arises due to mismatches between the energy transfer rate and the dissipation rate on small scales. Thus, before the onset of the dissipation range, an increase in energy occurs on intermediate scales, within the enstrophy cascade range, where the Kolmogorov scale breaks. It is interpreted as associated with nonlinear interactions, with energies temporarily accumulating before being dissipated on small scales.

In all processes examined, many dipoles and turbulent flows are observed in the binary mixture, in the onset of instabilities, which induce spontaneous occurrence of vortex dipoles followed by sound-wave (phonon) production. Following spectral analyses, all the instability cases were confronted with the expected classical scaling law behaviors. The Kolmogorov's scaling  $k^{-5/3}$  behavior, expected in the kinetic energy interval in which the wave number is smaller than the inverse of the healing length ( $k < 1/\xi$ ), is approximately confirmed in particular time intervals when the instabilities are emerging. This behavior appears to be more limited in the time interval for the RT case, which we interpret as being due to the two-step perturbation procedure leading to strong compressible density fluctuations during the initial dynamics. In the ultraviolet region (for  $k > 1/\xi$ ), the  $k^{-3}$  behavior is recognized at specific times of the onset of instabilities for all the cases, particularly for the incompressible part of the energy. In the spectral analyses of the IMQT cases (when only the nonlinear interactions are suddenly modified), the expected classical Kolmogorov scaling behavior is also not followed in an intermediate region before the ultraviolet region, which is associated with a kind of "bottleneck effect".

In summary, in this work, we have presented numerical simulations of three kinds of instabilities in binary coupled BEC mixture, obtained by using the coupled GP formalism, initially prepared in immiscible configurations. The cases are understood as accessible for experimental realizations, considering the actual cold-atom facilities. The RT and KH instabilities are investigated by keeping the coupled condensates in immiscible configuration along the dynamics, whereas the IMQT instability is obtained by quenching the nonlinear two-body parameter, from immiscible to miscible configuration, considering two different initial conditions. Our main objective was to explore different kinds of engineered instabilities, in a comparative way, which can emerge when coupling two initial immiscible condensates. Several interesting aspects of the dynamics, such as those related to vortic-

ity in the long-term evolution or associated with interference patterns in the coupled densities, are highlighted, but such analyses are beyond the scope of the present work. Deep-focus investigations are demanding in such cases.

## ACKNOWLEDGEMENTS

We are very grateful to Prof. Ashton S. Bradley for the suggestions, as well as for the local support obtained by one of us (RKK) during part of the realization of this work. For partial support during the realization of this work, we also acknowledge the following funding agencies: Marsden Fund, Contract UOO1726 (RKK); Fundação de Amparo à Pesquisa do Estado de São Paulo [Projs. 2024/04174-8 (SS and LT) and 2024/01533-7 (AG and LT)]; and Conselho Nacional de Desenvolvimento Científico e Tecnológico [Procs. 304469/2019-0 (LT), and 306219/2022-0 (AG)].

- 
- [1] O. Reynolds, XXIX. An experimental investigation of the circumstances which determine whether the motion of water shall be direct or sinuous, and of the law of resistance in parallel channels, *Philos. Trans. R. Soc.* **174**, 935 (1883).
- [2] A. Sommerfeld, Ein Beitrag zur hydrodynamischen Erklärung der turbulenten Flüssigkeitsbewegung, in: *Proc. of the 4th Int. Mathematical Congress, Rome 1908*, **3**, 116 (1909).
- [3] M. Eckert, The troublesome birth of hydrodynamic stability theory: Sommerfeld and the turbulence problem, *Eur. Phys. J. H* **35**, 29 (2010).
- [4] A. N. Kolmogorov, The local structure of turbulence in incompressible viscous fluid for very large Reynolds' numbers, *Dokl. Akad. Nauk SSSR* **30**, 301 (1941).
- [5] U. Frisch, *Turbulence: The Legacy of A. N. Kolmogorov*, Cambridge University Press, Cambridge, 1995.
- [6] R. J. Donnelly and C. E. Swanson, Quantum turbulence, *J. Fluid Mech.* **173**, 387 (1986).
- [7] C. F. Barenghi, Is the Reynolds number infinite in superfluid turbulence?, *Physica D* **237 D**, 2195 (2008).
- [8] A. S. Bradley and B. P. Anderson, Energy spectra of vortex distributions in two-dimensional quantum turbulence, *Phys. Rev. X* **2**, 041001 (2012).
- [9] M. T. Reeves, T. P. Billam, B. P. Anderson, and A. S. Bradley, Identifying a superfluid Reynolds number via dynamical similarity, *Phys. Rev. Lett.* **114**, 155302 (2015).
- [10] R. J. Donnelly, *Quantized Vortices in Helium II* (Cambridge University Press, Cambridge, England, 1991).
- [11] D. Jou and M. Sciacca, Quantum Reynolds number for superfluid counterflow turbulence, *Bollettino di Matematica Pura e Applicata* (M. S. Mongioví, M. Sciacca, and S. Triolo, eds.), vol. VI, pp. 95–103, Aracne editrice, 2013.
- [12] M. S. Mongioví, D. Jou, and M. Sciacca, Non-equilibrium thermodynamics, heat transport and thermal waves in laminar and turbulent superfluid helium, *Phys. Rep.* **726**, 1 (2018).
- [13] W. F. Vinen and J. J. Niemela, Quantum turbulence, *J. Low Temp. Phys.* **128**, 167 (2002).
- [14] M. S. Paoletti and D. P. Lathrop, Quantum turbulence, *Annu. Rev. Condens. Matter Phys.* **2**, 213 (2011).
- [15] M. Tsubota, M. Kobayashi, H. Takeuchi, Quantum hydrodynamics, *Phys. Rep.* **522**, 191 (2013).
- [16] S. K. Nemirovskii, Quantum turbulence: Theoretical and numerical problems, *Phys. Rep.* **524**, 85 (2013).
- [17] W.J. Kwon, G. Moon, J.Y. Choi, S.W. Seo, Y.-i. Shin, Relaxation of superfluid turbulence in highly oblate Bose–Einstein condensates, *Phys. Rev. A* **90**, 063627 (2014).
- [18] C. F. Barenghi and N. G. Parker, *A Primer on Quantum Fluids*, Springer International Publ., Switzerland, 2016.
- [19] M. C. Tsatsos, P. E. S. Tavares, A. Cidrim, A. R. Fritsch, M. A. Caracanhas, F. E. A. dos Santos, C. F. Barenghi, and V. S. Bagnato, Quantum turbulence in trapped atomic Bose–Einstein condensates, *Phys. Rep.* **622**, 1 (2016).
- [20] C. F. Barenghi, L. Skrbek, and K. R. Sreenivasan, *Quantum Turbulence*, Cambridge University Press, Cambridge, 2023.
- [21] M. Zhao, J. Tao, and I. B. Spielman, Kolmogorov Scaling in Turbulent 2D Bose-Einstein Condensates, *Phys. Rev. Lett.* **134**, 083402 (2025).
- [22] T. Z. Fischer and A. S. Bradley, Regimes of steady-state turbulence in a quantum fluid, *Phys. Rev. A* **111**, 023308 (2025).
- [23] S. Simjanovski, G. Gauthier, H. Rubinsztein-Dunlop, M. T. Reeves, and T. W. Neely, Shear-induced decaying turbulence in Bose-Einstein condensates, *Phys. Rev. A* **111**, 023314 (2025).
- [24] M. Tsubota, K. Fujimoto, S. Yui, Numerical studies of quantum turbulence, *J. Low Temp. Phys.* **188**, 119 (2017).
- [25] M. Kobayashi, P. Parnaudeau, F. Luddens, C. Lothodé, L. Danaila, M. Brachet, and I. Danaila, Quantum turbulence simulations using the Gross-Pitaevskii equation: high-performance computing and new numerical benchmarks, *Comput. Phys. Commun.* **258**, 107579 (2021).
- [26] W. F. Vinen, Mutual friction in a heat current in liquid helium II I. Experiments on steady heat currents, *Proc. R. Soc.* **240**, 114 (1957); Mutual friction in a heat current in liquid helium II. II. Experiments on transient effects, *Proc. R. Soc.* **240**, 128 (1957); Mutual friction in a heat current in liquid helium II III. Theory of the mutual friction **242**, 493 (1957).
- [27] E. A. L. Henn, J. A. Seman, G. Roati, K. M. F. Magalhães, and V. S. Bagnato, Emergence of turbulence in an oscillating Bose-Einstein condensate, *Phys. Rev. Lett.* **103**, 045301 (2009).

- [28] A. C. White, B. P. Anderson, and V. S. Bagnato, Vortices and turbulence in trapped atomic condensates, *PNAS* **111**, 4719 (2014).
- [29] N. Navon, A. L. Gaunt, R. P. Smith, and Z. Hadzibabic, Emergence of a turbulent cascade in a quantum gas, *Nature* **539**, 72 (2016).
- [30] M. T. Reeves, K. Goddard-Lee, G. Gauthier, O. R. Stockdale, H. Salman, T. Edmonds, X. Yu, A. S. Bradley, M. Baker, H. Rubinsztein-Dunlop, M. J. Davis, and T. W. Neely, Turbulent relaxation to equilibrium in a two-dimensional quantum vortex gas, *Phys. Rev. X* **12**, 011031 (2022).
- [31] G. Gauthier, M. T. Reeves, X. Yu, A. S. Bradley, M. Baker, T. A. Bell, H. R. Dunlop, M. J. Davis, and T. W. Neely, Giant vortex clusters in a two-dimensional quantum fluid, *Science* **364**, 1264 (2019).
- [32] S. P. Johnstone, A. J. Groszek, P. T. Starkey, C. J. Billington, T. P. Simula, and K. Helmerson, Evolution of large-scale flow from turbulence in a two-dimensional superfluid, *Science* **364**, 1267 (2019).
- [33] C. Nore, M. Abid, and M. E. Brachet, Kolmogorov turbulence in low-temperature superflows, *Phys. Rev. Lett.* **78**, 3896 (1997).
- [34] M. Kobayashi and M. Tsubota, Kolmogorov spectrum of superfluid turbulence: Numerical analysis of the Gross-Pitaevskii equation with a small-scale dissipation, *Phys. Rev. Lett.* **94**, 065302 (2005).
- [35] J. Yepez, G. Vahala, L. Vahala, and M. Soe, Superfluid turbulence from quantum Kelvin wave to classical Kolmogorov cascades *Phys. Rev. Lett.* **103**, 084501 (2009).
- [36] A. W. Baggaley and C. F. Barenghi, Spectrum of turbulent Kelvin-waves cascade in superfluid helium, *Phys. Rev. B* **83**, 134509 (2011).
- [37] M. T. Reeves, T. P. Billam, B. P. Anderson and A. S. Bradley, Inverse energy cascade in forced two-dimensional quantum turbulence, *Phys. Rev. Lett.* **110**, 104501 (2013).
- [38] M. T. Reeves, T. P. Billam, B. P. Anderson and A. S. Bradley, Signatures of coherent vortex structures in a disordered two-dimensional quantum fluid, *Phys. Rev. A* **89**, 053631 (2014).
- [39] D. S. Hall, M. R. Matthews, J. R. Ensher, C. E. Wieman, and E. A. Cornell, Dynamics of Component Separation in a Binary Mixture of Bose-Einstein Condensates, *Phys. Rev. Lett.* **81**, 1539 (1998).
- [40] C. J. Pethick and H. Smith, *Bose-Einstein Condensation in Dilute Gases* (Cambridge University Press, Cambridge, 2002).
- [41] R. K. Kumar, P. Muruganandam, L. Tomio, and A. Gammal, Miscibility in coupled dipolar and non-dipolar Bose-Einstein condensates, *J. Phys. Commun.* **1**, 035012 (2017).
- [42] L. Rayleigh, *Scientific Papers, Vol. II* (Cambridge Univ. Press, Cambridge, England, 1900), 200.
- [43] G. I. Taylor, The instability of liquid surfaces when accelerated in a direction perpendicular to their planes, *Proc. R. Soc. London Ser. A* **201**, 192 (1950).
- [44] W. Thompson (Lord Kelvin), Hydrokinetic solutions and observations, *Philos. Mag.* **42** 362 (1871); **10**, 155 (1980).
- [45] H. von Helmholtz, Über discontinuierliche Flüssigkeits-Bewegungen, *Monatsberichte der Königlich Preussische Akademie der Wissenschaften zu Berlin* **23**, 215 (1868).
- [46] D. H. Sharp, An overview of Rayleigh-Taylor instability, *Physica D* **12**, 3 (1984).
- [47] A. Banerjee, Rayleigh-Taylor instability: A status review of experimental designs and measurement diagnostics, *J. Fluids Eng.* **142**, 120801 (2020).
- [48] R. Blaauwgeers, V. B. Eltsov, G. Eska, A. P. Finne, R. P. Haley, M. Krusius, J. J. Ruohio, L. Skrbek, and G. E. Volovik, Shear flow and Kelvin-Helmholtz instability in superfluids, *Phys. Rev. Lett.* **89**, 155301 (2002).
- [49] A. P. Finne, V. B. Eltsov, R. Hänninen, N. B. Kopnin, J. Kopu, M. Krusius, M. Tsubota and G. E. Volovik, Dynamics of vortices and interfaces in superfluid  $^3\text{He}$ , *Rep. Prog. Phys.* **69**, 3157 (2006).
- [50] N. G. Berloff and C. Yin, Turbulence and coherent structures in two-component Bose condensates, *J. Low Temp. Phys.* **145**, 187 (2006).
- [51] K. Sasaki, N. Suzuki, D. Akamatsu, and H. Saito, Rayleigh-Taylor instability and mushroom-pattern formation in a two-component Bose-Einstein condensate, *Phys. Rev. A* **80**, 063611 (2009).
- [52] H. Takeuchi, N. Suzuki, K. Kasamatsu, H. Saito, and M. Tsubota, Quantum Kelvin-Helmholtz instability in phase-separated two-component Bose-Einstein condensates, *Phys. Rev. B* **81**, 094517 (2010).
- [53] A. Bezett, V. Bychkov, E. Lundh, D. Kobayakov, and M. Marklund, Magnetic Richtmyer-Meshkov instability in a two-component Bose-Einstein condensate, *Phys. Rev. A* **82**, 043608 (2010).
- [54] D. Kobayakov, V. Bychkov, E. Lundh, A. Bezett, V. Akkerman, and M. Marklund, Interface dynamics of a two-component Bose-Einstein condensate driven by an external force, *Phys. Rev. A* **83**, 043623 (2011).
- [55] D. Kobayakov, A. Bezett, E. Lundh, M. Marklund, and V. Bychkov, Turbulence in binary Bose-Einstein condensates generated by highly nonlinear Rayleigh-Taylor and Kelvin-Helmholtz instabilities, *Phys. Rev. A* **89**, 013631 (2014).
- [56] K. Fujimoto and M. Tsubota, Direct and inverse cascades of spin-wave turbulence in spin-1 ferromagnetic spinor Bose-Einstein condensates, *Phys. Rev. A* **93**, 033620 (2016).
- [57] T. Mithun, K. Kasamatsu, B. Dey, and P. G. Kevrekidis, Decay of two-dimensional quantum turbulence in binary Bose-Einstein condensates, *Phys. Rev. A* **103**, 023301 (2021).
- [58] H. Kokubo, K. Kasamatsu, and H. Takeuchi, Pattern formation of quantum Kelvin-Helmholtz instability in binary superfluids, *Phys. Rev. A* **104**, 023312 (2021).
- [59] A. Saboo, s. Halder, S. Das, and S. Majumder, Rayleigh-Taylor instability in a phase-separated three-component Bose-Einstein condensate, *Phys. Rev. A* **108**, 013320 (2023).
- [60] A. N. da Silva, R. K. Kumar, A. S. Bradley, and L. Tomio, Vortex generation in stirred binary Bose-Einstein condensates, *Phys. Rev. A* **107**, 033314 (2023).
- [61] T. Kadokura and H. Saito, Kolmogorov-Hinze scales in turbulent superfluids, *Phys. Rev. Lett.* **133**, 256001 (2024).
- [62] N. Bigagli, W. Yuan, S. Zhang, B. Bulatovic, T. Karman, I. Stevenson, and S. Will, Observation of Bose-Einstein condensation of dipolar molecules, *Nature* **631**, 289 (2024).
- [63] S. Sabari, R. K. Kumar, L. Tomio, Vortex dynamics and turbulence in dipolar Bose-Einstein condensates, *Phys.*



- Rev. A **109**, 023313 (2024).
- [64] S. Sabari and R. K. Kumar, Effect of an oscillating Gaussian obstacle in a dipolar Bose-Einstein condensate, *Eur. Phys. J. D* **72**, 48 (2018).
- [65] L. Tomio, A. N. da Silva, S. Sabari, R. K. Kumar, Dynamical vortex production and quantum turbulence in perturbed Bose-Einstein condensates, *Few-Body Systems* **65**, 13 (2024).
- [66] D. Kivotides, C. F. Barenghi, and D. C. Samuels, Fractal dimension of superfluid turbulence, *Phys. Rev. Lett.* **87**, 155301 (2001).
- [67] S. V. Koniakhin, O. Bleu, G. Malpuech, and D. D. Solnyshkov, 2D quantum turbulence in a polariton quantum fluid, *Chaos, Solitons and Fractals* **132**, 109574 (2019).
- [68] P. Constantin, C. Foias, O. P. Manley and R. Temam, Determining modes and fractal dimension of turbulent flows, *J. Fluid Mech.* **150**, 427 (1985).
- [69] G. R. Rakhshandehroo, M. R. Shaghaghian, A. R. Keshavarzi, N. Talebbeydokhti, Temporal variation of velocity components in a turbulent open channel flow: Identification of fractal dimensions, *Appl. Math. Model.* **33**, 3815 (2009).
- [70] Y. Geng, J. Tao, S. Mukherjee, S. Eckel, G. K. Campbell, and I. B. Spielman, The Rayleigh-Taylor instability in a binary quantum fluid, arXiv: 2411.19807v1.
- [71] F. A. Bayocboc Jr., J. Dziarmaga, and W. H. Zurek, Biased dynamics of the miscible-immiscible quantum phase transition in a binary Bose-Einstein condensate, *Phys. Rev. B* **109**, 064501 (2024).
- [72] K. Mukherjee, S. I. Mistakidis, P. G. Kevrekidis, and P. Schmelcher, Quench induced vortex-bright-soliton formation in binary Bose-Einstein condensates, *J. Phys. B: At. Mol. Opt. Phys.* **53**, 055302 (2020).
- [73] Y. Eto, M. Takahashi, M. Kunimi, H. Saito, and T. Hirano, Nonequilibrium dynamics induced by miscible-immiscible transition in binary Bose-Einstein condensates, *New J. Phys.* **18**, 073029 (2016).
- [74] K. Kasamatsu and M. Tsubota, Multiple Domain Formation Induced by Modulation Instability in Two-Component Bose-Einstein Condensates, *Phys. Rev. Lett.* **93**, 100402 (2004).
- [75] R.T. Thiruvalluvar, E. Wamba, S. Sabari, K. Porsezian, Impact of higher-order nonlinearity on modulational instability in two-component Bose-Einstein condensates, *Phys. Rev. E* **99**, 032202 (2019).
- [76] A. S. Bradley, R. K. Kumar, S. Pal, and X. Yu, Spectral analysis for compressible quantum fluids, *Phys. Rev. A* **106**, 043322 (2022).
- [77] E. Timmermans, P. Tommasini, M. Hussein, and A. Kerman, Feshbach resonances in atomic Bose-Einstein condensates, *Phys. Rep.* **315**, 199 (1999).
- [78] C. Chin, R. Grimm, P. Julienne, and E. Tiesinga, Feshbach resonances in ultracold gases, *Rev. Mod. Phys.* **82**, 1225 (2010).
- [79] R. K. Kumar, L. Tomio, and A. Gammal, Vortex patterns in rotating dipolar Bose-Einstein condensate mixtures with squared optical lattices, *J. Phys. B: At. Mol. Opt. Phys.* **52**, 025302 (2019).
- [80] R. K. Kumar, A. Gammal, and L. Tomio, Mass-imbalanced Bose-Einstein condensed mixtures in rotating perturbed trap, *Phys. Lett. A* **384**, 126535 (2020).
- [81] S. Huh, W. Yun, G. Yun, S. Hwang, K. Kwon, J. Hur, S. Lee, H. Takeuchi, S. K. Kim, and J.-Y. Choi, Beyond skyrmion spin texture from quantum Kelvin-Helmholtz instability, arXiv: 2408.11217v1.
- [82] D. J. McCarron, H. W. Cho, D. L. Jenkin, M. P. Köpinger and S. L. Cornish, Dual-species Bose-Einstein condensate of  $^{87}\text{Rb}$  and  $^{133}\text{Cs}$ , *Phys. Rev. A* **84**, 011603(R) (2011).
- [83] E. Kozik and B. Svistunov, Vortex-phonon interaction, *Phys. Rev. B* **72**, 172505 (2005).
- [84] J. T. Mendonça, F. Haas and A. Gammal, Nonlinear vortex-phonon interactions in a Bose-Einstein condensate, *J. Phys. B: At. Mol. Opt. Phys.* **49**, 145302 (2016).
- [85] A. S. Bradley, Dunedin, New Zealand, 2018, [//github.com/AshtonSBradley/VortexDistributions.jl](https://github.com/AshtonSBradley/VortexDistributions.jl).
- [86] For the IMQT the initial immiscible configuration was assumed with  $\delta = 1.02$  in the first case, with  $\delta = 1.05$  in the second case, to verify the effect of a slightly different  $\delta$  in the observed interference fringes of the densities [See panels (c<sub>i</sub>) and (d<sub>i</sub>) of Figs. 8 and 11]. The effect of changing  $\delta$  is further discussed in the time evolution of the overlap  $\Lambda$ , shown in Fig. 14.
- [87] M. R. Andrews, C. G. Townsend, H.-J. Miesner, D. S. Durfee, D. M. Kurn, and W. Ketterle, Observation of interference between two Bose condensates, *Science* **275**, 637 (1997).
- [88] D. J. Frantzeskakis, Dark solitons in atomic Bose-Einstein condensates: from theory to experiments, *J. Phys. A: Math. Theor.* **43**, 213001 (2010).
- [89] D. E. Pelinovsky, Y. A. Stepanyants, and Y. S. Kivshar, Self-focusing of plane dark solitons in nonlinear defocusing media, *Phys. Rev. E* **51**, 5016 (1995).
- [90] G. A. El, A. Gammal, and A. M. Kamchatnov, Oblique Dark Solitons in Supersonic Flow of a Bose-Einstein Condensate, *Phys. Rev. Lett.* **97**, 180405 (2006).
- [91] D. Yan, J. J. Chang, C. Hamner, M. Hoefler, P. G. Kevrekidis, P. Engels, V. Achilleos, D. J. Frantzeskakis, and J. Cuevas, Beating dark-dark solitons in Bose-Einstein condensates, *J. Phys. B: At. Mol. Opt. Phys.* **45**, 115301 (2012).
- [92] V. Tikhonenko, J. Christou, B. Luther-Davies, and Y. S. Kivshar, Observation of vortex solitons created by the instability of dark soliton stripes, *Opt. Lett.* **21**, 1129 (1996).
- [93] C. Connaughton and S. V. Nazarenko, Warm cascades and Anomalous Scaling in a Diffusion Model of Turbulence, *Phys. Rev. Lett.* **92**, 044501 (2004).
- [94] V. S. L'vov, S. V. Nazarenko, and O. Rudenko, Bottleneck crossover between classical and quantum superfluid turbulence, *Phys. Rev. B* **76**, 024520 (2007).
- [95] A. del Río-Lima, J. A. Seman, R. Jáuregui, and F. J. Poveda-Cuevas, Spatial and temporal periodic density patterns in driven Bose-Einstein condensates, *Phys. Rev. A* **110**, 053318 (2024).